

# Vibrational and vibronic structure of isolated point defects: the nitrogen–vacancy center in diamond

Lukas Razinkovas,<sup>1,\*</sup> Marcus W. Doherty,<sup>2</sup> Neil B. Manson,<sup>2</sup> Chris G. Van de Walle,<sup>3</sup> and Audrius Alkauskas<sup>1</sup>

<sup>1</sup>*Center for Physical Sciences and Technology (FTMC), Vilnius LT-10257, Lithuania*

<sup>2</sup>*Laser Physics Centre, Research School of Physics, Australian National University, Canberra, Australian Capital Territory 2601, Australia*

<sup>3</sup>*Materials Department, University of California, Santa Barbara, California 93106-5050, USA*

(Dated: June 16, 2022)

We present a theoretical study of vibrational and vibronic properties of a point defect in the dilute limit by means of first-principles density functional theory calculations. As an exemplar we choose the negatively charged nitrogen–vacancy center, a solid-state system that has served as a testbed for many protocols of quantum technology. We achieve low effective concentrations of defects by constructing dynamical matrices of large supercells containing tens of thousands of atoms. The main goal of the paper is to calculate luminescence and absorption lineshapes due to coupling to vibrational degrees of freedom. The coupling to symmetric  $a_1$  modes is computed via the Huang–Rhys theory. Importantly, to include a nontrivial contribution of  $e$  modes we develop an effective methodology to solve the multi-mode  $E \otimes e$  Jahn–Teller problem. Our results show that for NV centers in diamond a proper treatment of  $e$  modes is particularly important for absorption. We obtain good agreement with experiment for both luminescence and absorption. Finally, the remaining shortcomings of the theoretical approach are critically reviewed. The presented theoretical approach will benefit identification and future studies of point defects in solids.

## I. INTRODUCTION

The calculation of optical lineshapes of point defects in solids is a topic with long history [1–4]. Yet, atomistic first-principles calculations [5] have been difficult. Certain properties of defects, such as discrete energy levels or localized magnetic moments, resemble those of atoms or molecules. However, those localized states are surrounded by a huge number of other electrons and ions, which makes point defects qualitatively different from atoms and molecules and requires a treatment as a solid-state system. Unfortunately, unlike perfect crystals, defects do not possess translational symmetry, which significantly complicates their quantum-mechanical description.

Optical signatures of defects in semiconductors and insulators are properties where both the atomic and the solid-state aspects are manifest. Many defects have localized levels in the band gap of the host material, on par with atoms or molecules in vacuum. Optical transitions involving those levels usually lead to lattice rearrangement. This rearrangement typically couples to a continuum of vibrational modes with different frequencies, in contrast to molecules, where a finite number of vibrations participate. As a result, optical signatures of defects are composed of continuous *bands* [4].

Due to the complexity of the problem earlier first-principles calculations of optical bands involved approximations that were not fully tested. Kretov *et al.* [6] performed a study of the luminescence lineshape of a Mn impurity in  $\text{Zn}_2\text{SiO}_4$ , but approximated the vibrational modes of the defect system by those of the bulk

crystal. Alkauskas *et al.* calculated luminescence lineshapes of defects in GaN and ZnO with a very strong electron–phonon coupling (as quantified by the so-called Huang–Rhys factor [1]  $S \gg 1$ , discussed below) [7]. For such systems optical lineshapes can be accurately calculated by mapping all vibrations onto an effective one-dimensional vibrational problem [1]. In subsequent work, Alkauskas *et al.* calculated the luminescence lineshape for a negatively charged nitrogen–vacancy (NV) center in diamond [8], a defect in which electron–phonon coupling is not strong enough to justify the single-mode approximation. They explicitly treated all phonons pertaining to the defect system by diagonalizing dynamical matrices of periodically repeated supercells [9] with up to 11 000 atoms. The calculations took into account only symmetric  $a_1$  vibrational modes, whereas it is known that asymmetric  $e$  modes also contribute [10] due to the dynamical Jahn–Teller (JT) effect in the electronically excited state [11]. A few other recent studies have calculated optical lineshapes of point defects [12–14]. Most of the published work used fairly small supercells, which yields an incomplete description of the phonon spectrum. It can be concluded that the status of calculations of optical lineshapes of point defects is much behind that of molecules where very accurate calculations are now being routinely performed [15–17].

A proper inclusion of the dynamical JT effect is very difficult. Historically, an understanding of this effect has been achieved by invoking an effective single-mode approximation for the degenerate asymmetric vibrational mode [18]. This approximation suffices to obtain the general features of optical lineshapes [19] or to assess the effect of the JT interaction on spin–orbit coupling [20]. However, the single-mode approach is insufficient in the case of defects with weak to moderate electron–phonon

\* lukas.razinkovas@ftmc.lt

coupling. Unfortunately, the problem of diagonalizing the vibronic (*i.e.*, combined vibrational and electronic) Hamiltonian has an extremely unfavorable scaling with regard to the number of vibrational modes that are included. In the past, this limited the consideration of the dynamical JT effect to no more than just a few vibrational degrees of freedom [21].

In this work, we present first-principles calculations of defect optical lineshapes for the NV center in diamond. The NV center is a very useful model system because its structure is accurately known and the defect is extremely well characterized spectroscopically. Our present work goes well beyond the ideas developed in Ref. 8 and significantly advances the methodology and calculations in the following areas: (i) We present the calculations of absorption lineshapes in addition to luminescence lineshapes. (ii) The contribution of asymmetric  $e$  vibrations is included. The latter is possible since (iii) we propose and test an efficient algorithm to solve the multi-mode Jahn–Teller problem, which allows us to treat vibronic coupling to a very large number of asymmetric modes.

Our work is not just an academic exercise in the development of quantum-mechanical methods for solid-state systems. Recently, the field of point defects in solids has experienced a renaissance due to the application of point defects in various branches of quantum technologies: quantum computing, quantum communication, and quantum sensing [22]. While the NV center is probably one of the most prominent examples of these so-called quantum defects, many other defects have been addressed [22]. There is a wealth of experimental data on various point defects in solids and many potentially useful systems await to be discovered or identified. The ability to accurately calculate optical signatures of point defects will greatly aid their identification and potential application. We note that the dynamic Jahn–Teller effect influences not only the vibrational sidebands but also the fine structure of the spectra, in particular the splitting of the zero-phonon line (ZPL, see below for a definition). In the case of the NV center the fine structure is affected by the spin-orbit coupling in the excited state, which, in its turn, is reduced when the dynamic Jahn–Teller effect is present [20]. The fine structure of the spectra will not be considered in this work.

The paper is organized as follows. In Sec. II we introduce the nitrogen–vacancy center. In Sec. III the general theory of optical lineshapes of defects is laid down. The first-principles methodology and actual calculations are presented in Sec. IV. These calculations are subsequently used to build effective models of NV centers in very large supercells, as detailed in Sec. V. Coupling to fully symmetric  $a_1$  vibrational modes is discussed in Sec. VI and the interaction with  $e$  modes, *i.e.*, the dynamical multi-mode Jahn–Teller effect, is analyzed in Sec. VII. The calculated lineshapes, where the contributions of  $a_1$  and  $e$  modes are combined, are presented and compared to experiments in Sec. VIII. Our findings are summarized in Sec. IX, where we also discuss possible sources of the

remaining small discrepancies between theory and experiment.

## II. THE NITROGEN–VACANCY CENTER

The defect studied in this paper is the negatively charged nitrogen–vacancy (NV) center in diamond, depicted in Fig. 1(a). It is a complex of a substitutional nitrogen atom with a carbon vacancy; the extra electron comes from remote donors. Over the past two decades the NV center has been the focus of a lot of research activity [10] due to its application in nanoscale sensing [23], quantum communication [24], and quantum computation [25].

The point-group symmetry of the defect is  $C_{3v}$  with a three-fold axis going through the nitrogen and the vacant site. The energy level diagram of the negatively charged NV center is shown in Fig. 1(b). The NV center has a triplet ground state  $^3A_2$  and a triplet excited state  $^3E$ . Once the system is in the excited state, it can either return to the ground state via a radiative transition or undergo an inter-system crossing to the singlet state  $^1A_1$ . The latter process is important for optical spin polarization and read-out; for more details see Ref. 10. In this paper, we will focus on optical transitions between  $^3E$  and  $^3A_2$  states. Also, we will use the term “NV center” omitting the explicit mention of its negative charge state.

The role of lattice vibrations in optical properties can be qualitatively illustrated using an effective one-dimensional (1D) representation, the so-called configuration coordinate diagram [4, 26], shown in Fig. 1(c). The equilibrium geometries of the defect in the excited and the ground state are different, which is reflected by the fact that total energies in different electronic states attain their minimum for different configurations. In the so-called classical Franck–Condon picture the energy  $E_{\text{abs}}$  is associated with absorption energy and the energy  $E_{\text{em}}$  with emission. Lattice relaxation energies during optical transitions are quantified by Franck–Condon shifts in the ground ( $\Delta E_g$ ) and the excited ( $\Delta E_e$ ) state.

Let the energy difference between the equilibrium configurations be  $E_0$  and let  $\varepsilon_{gn}$  and  $\varepsilon_{em}$  be energy eigenvalues of quantum-mechanical vibronic levels in the ground and the excited state, referenced to the respective potential energy minima. The optical transition between the lowest vibronic level in the excited state and the lowest vibronic level in the ground state is called the zero-phonon line (ZPL); its energy is

$$E_{\text{ZPL}} = E_0 + \varepsilon_{e0} - \varepsilon_{g0}. \quad (1)$$

The zero-phonon line is the transition during which the net number of phonons in the system does not change. Strictly speaking, the definition Eq. (1) is valid only for  $T = 0$  K. In this paper we will assume this low-temperature limit and calculate luminescence and absorption lineshapes for  $T = 0$  K.

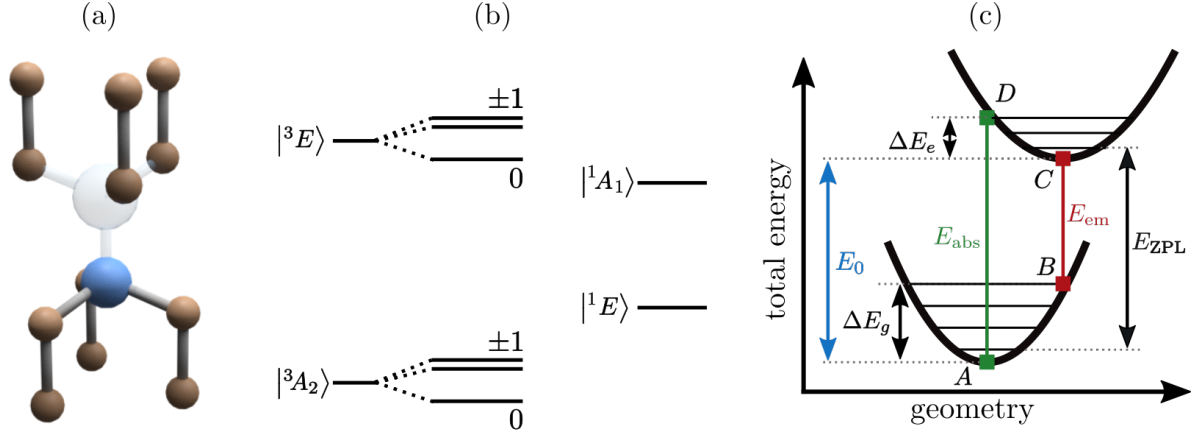


FIG. 1. (a) Atomic structure of the NV center in diamond. (b) Energy-level diagram of the NV center. Splitting of the magnetic sub-levels is not to scale. (c) One-dimensional representation of adiabatic potential energy surfaces in the ground and the excited states. Points A and D represent equilibrium geometry of the ground state, while points B and C represent equilibrium geometry of the excited state.  $\Delta E_g$  and  $\Delta E_e$  are lattice relaxation energies.  $E_0$  is energy difference between the potential energy minima, and  $E_{\text{ZPL}}$  is the energy of the zero-phonon line.

Because of different geometries in the excited and the ground state, luminescence and absorption signals are not narrow lines at the energy of the ZPL, but become broadened due to lattice vibrations, resulting in bands. A quantitative theory of the vibrational structure of optical lines is given next, in Sec. III.

### III. VIBRATIONAL BROADENING OF OPTICAL TRANSITIONS

The process of optical emission is described by an energy-dependent emission probability  $P(\hbar\omega)$ , number of photons emitted in the solid angle  $4\pi$  per unit energy per unit time. The process of absorption is described by an absorption cross section  $\sigma(\hbar\omega)$ . These quantities are given by [27]:

$$P(\hbar\omega) = C_P \omega^3 I_{\text{em}}(\hbar\omega); \quad \sigma(\hbar\omega) = C_\sigma \omega I_{\text{abs}}(\hbar\omega), \quad (2)$$

where

$$I_{\text{em}}(\hbar\omega) = \sum_n |\langle \Psi_{e0} | \hat{\mu} | \Psi_{gn} \rangle|^2 \delta(E_0 + \varepsilon_{e0} - \varepsilon_{gn} - \hbar\omega), \quad (3)$$

and

$$I_{\text{abs}}(\hbar\omega) = \sum_n |\langle \Psi_{g0} | \hat{\mu} | \Psi_{en} \rangle|^2 \delta(E_0 + \varepsilon_{en} - \varepsilon_{g0} - \hbar\omega). \quad (4)$$

In the subscripts  $g$  stands for “ground” and  $e$  for “excited”.  $C_P$  and  $C_\sigma$  contain fundamental physical constants, as well as the refractive index of diamond,  $n_r$ . As we will be interested in normalized lineshapes, these constants will not be discussed further. Wavefunctions  $|\Psi_{gn}\rangle$  and  $|\Psi_{en}\rangle$  describe vibronic states in the ground

and excited electronic manifolds; their energies  $\varepsilon_{gn}$  and  $\varepsilon_{en}$  were introduced in Sec. II.  $\hat{\mu}$  is the dipole operator; in the most general case it can be written as the sum of electronic and ionic contributions:

$$\hat{\mu} = \hat{\mu}_{el} + \hat{\mu}_N. \quad (5)$$

In this paper we will employ the so-called crude adiabatic (also called static) approximation. In this approximation electronic wavefunctions depend only on electronic degrees of freedom and they are eigenfunctions of the electronic Hamiltonian corresponding to some fixed position of ions [28].

The ground state of the NV center is an orbital singlet [10], and its vibronic states can be written as:

$$|\Psi_{g;pr}\rangle = \chi_{gp}^{a_1}(\mathbf{Q}_{a_1}) \chi_{gr}^e(\mathbf{Q}_e) |A_2\rangle. \quad (6)$$

Here the  $a_1$  and  $e$  symmetry components of the vibrational wavefunction are shown explicitly. To describe these components we need two quantum numbers  $p$  and  $r$  that in the previous expressions were substituted with a single index  $n$ . To avoid possible confusion the index ‘ $e$ ’ for ‘excited’ will be used as a subscript, and the index ‘ $e$ ’ to label the  $e$  irreducible representation will be used as a superscript whenever both indices appear on the same symbol.

The excited state is an orbital doublet [10], and the general expression of its vibronic states is [29]:

$$|\Psi_{e;st}\rangle = \chi_{es}^{a_1}(\mathbf{Q}_{a_1}) [\chi_{et}^{e_x}(\mathbf{Q}_e) |E_x\rangle + \chi_{et}^{e_y}(\mathbf{Q}_e) |E_y\rangle], \quad (7)$$

where  $s$  and  $t$  are used to label ionic wavefunctions of  $a_1$  and  $e$  symmetry, respectively; like for the ground state, quantum numbers  $s$  and  $t$  replace a single quantum number  $n$  in Eq. (4). Using the notation

$$|\Phi_{et}\rangle = \chi_{et}^{e_x}(\mathbf{Q}_e) |E_x\rangle + \chi_{et}^{e_y}(\mathbf{Q}_e) |E_y\rangle \quad (8)$$

we can rewrite the vibronic wavefunction in the excited state as:

$$|\Psi_{e;st}\rangle = \chi_{es}^{a_1}(\mathbf{Q}_{a_1}) |\Phi_{et}\rangle. \quad (9)$$

This form will be useful in Sec. VII.

In the expressions above ionic wavefunctions pertaining to vibrational modes of  $a_2$  symmetry are not explicitly shown. In the case of the NV center these modes show up neither in absorption nor emission. The reason for this is that the difference between equilibrium geometries in the  ${}^3A_2$  and  ${}^3E$  electronic states (to be discussed in more detail in Secs. VI and VII) contains only  $a_1$  and  $e$  components, but no  $a_2$  components. I.e., the projection of that difference on  $a_2$  vibrational modes is zero. Thus, these modes will not be considered further in this work. However,  $a_2$  modes can in principle contribute in some other  $C_{3v}$  systems. As these modes do not break the degeneracy of  $E$  electronic states, they are not Jahn-Teller active. Therefore, they can be treated the same way as  $a_1$  modes.

When ground and excited state wavefunctions are in the form of Eqs. (6) and (7), the nuclear part of the dipole operator [Eq. (5)] does not contribute. If the symmetry axis of the NV center is along the  $z$  direction, then light emitted from this center is polarized in the  $xy$  plane. Using group-theoretical analysis one can then show that

$$\begin{aligned} & |\langle \Psi_{g;pr} | \hat{\mu}_{et} | \Psi_{e;st} \rangle|^2 \\ &= |\mu_0|^2 |\langle \chi_{gp}^{a_1} | \chi_{es}^{a_1} \rangle|^2 \left[ |\langle \chi_{gr}^e | \chi_{et}^e \rangle|^2 + |\langle \chi_{gr}^e | \chi_{et}^{e_y} \rangle|^2 \right] \end{aligned} \quad (10)$$

where  $\mu_0 = \sum_i e \langle A_2 | x_i | E_y \rangle$  is the reduced matrix element in the Wigner-Eckart theorem (the sum runs over all electrons of the negatively charged NV center and  $e$  is elementary charge). Physically,  $\mu_0$  is simply the transition dipole moment.

The energies of vibronic levels that appear in Eqs. (3) and (4) are a sum of contributions by  $a_1$  and  $e$  modes, i.e.  $\varepsilon_{gn} = \varepsilon_{gp}^{a_1} + \varepsilon_{gr}^e$  and similarly for the excited state. In this case one can show that functions  $I_{em}$  and  $I_{abs}$  from Eqs. (3) and (4) can be expressed as:

$$I_{\{em,abs\}}(\hbar\omega) = |\mu_0|^2 A_{\{em,abs\}}(\hbar\omega), \quad (11)$$

where  $A(\hbar\omega)$ , the spectral function, is given by the following expression:

$$A_{\{em,abs\}}(\hbar\omega) = \int A_{a_1}(\hbar\omega - \hbar\omega') A_e(\hbar\omega') d(\hbar\omega'). \quad (12)$$

This is a convolution of the two spectral functions pertaining to  $a_1$  and  $e$  modes. In the case of luminescence we define these spectral functions by:

$$A_{a_1}(\hbar\omega) = \sum_p |\langle \chi_{e0}^{a_1} | \chi_{gp}^{a_1} \rangle|^2 \delta(E_{ZPL} + \varepsilon_{g0}^{a_1} - \varepsilon_{gp}^{a_1} - \hbar\omega) \quad (13)$$

and

$$\begin{aligned} A_e(\hbar\omega) &= \sum_r \left[ |\langle \chi_{e0}^{e_x} | \chi_{gr}^e \rangle|^2 + |\langle \chi_{e0}^{e_y} | \chi_{gr}^e \rangle|^2 \right] \\ &\times \delta(\varepsilon_{g0}^e - \varepsilon_{gr}^e - \hbar\omega). \end{aligned} \quad (14)$$

In the case of absorption they are:

$$A_{a_1}(\hbar\omega) = \sum_s |\langle \chi_{es}^{a_1} | \chi_{g0}^{a_1} \rangle|^2 \delta(E_{ZPL} + \varepsilon_{es}^{a_1} - \varepsilon_{e0}^{a_1} - \hbar\omega) \quad (15)$$

and

$$\begin{aligned} A_e(\hbar\omega) &= \sum_t \left[ |\langle \chi_{et}^{e_x} | \chi_{g0}^e \rangle|^2 + |\langle \chi_{et}^{e_y} | \chi_{g0}^e \rangle|^2 \right] \\ &\times \delta(\varepsilon_{et}^e - \varepsilon_{e0}^e - \hbar\omega). \end{aligned} \quad (16)$$

Since  $A_{a_1}$  carries the lion's share of luminescence and absorption lineshapes (as discussed in Secs. VI, VII, and VIII), we choose to define  $A_{a_1}$  with respect to  $E_{ZPL}$ , while  $A_e$  is defined with respect to energy 0. This is done for convenience only and other choices are certainly possible. Therefore, in the case of emission  $A_{a_1}(\hbar\omega)$  is non-zero for energies smaller than  $E_{ZPL}$ , while  $A_e(\hbar\omega)$  is non-zero for energies smaller than 0. In the case of absorption  $A_{a_1}(\hbar\omega)$  is nonzero for energies larger than  $E_{ZPL}$ , and  $A_e(\hbar\omega)$  is nonzero for energies larger than 0. All quantities  $A(\hbar\omega)$  are automatically normalized to 1 as per their definition.

As mentioned above, in this work we will not deal with absolute luminescence intensities and absorption cross-sections, defined in Eq. (2), but rather with normalized lineshapes. Comparing with Eq. (2), we see that those are given by:

$$L_{em}(\hbar\omega) = N_1 \omega^3 A_{em}(\hbar\omega) \quad (17)$$

for emission and

$$L_{abs}(\hbar\omega) = N_2 \omega A_{abs}(\hbar\omega) \quad (18)$$

for absorption, where  $N_1$  and  $N_2$  are normalization constants, needed because of the appearance of factors  $\omega^3$  and  $\omega$  in  $L_{\{em,abs\}}(\hbar\omega)$ . The principal task of the current paper is the evaluation of Eqs. (12)–(18) for the NV center.

#### IV. FIRST-PRINCIPLES CALCULATIONS

Calculations have been performed within the framework of density functional theory (DFT). Exchange and correlation was described by the hybrid functional of Heyd, Scuseria, and Ernzerhof (HSE) [30]. In HSE a fraction  $a = 1/4$  of screened Fock exchange is admixed to the semi-local exchange based on the generalized gradient approximation (GGA) in the form of Perdew, Burke, and Ernzerhof (PBE) [31]. As discussed below, the HSE functional provides a very good description of the electronic structure of bulk diamond (in particular its band gap), and optical excitations energy of the NV center [32] (Sec. IV B). However, the PBE functional yields better agreement with experiment for the bulk lattice constant, the bulk modulus, and the vibrational properties of diamond [33] (Sec. IV A). For this reason we also perform



TABLE I. Calculated lattice constants  $a$  (Å), bulk moduli  $B$  (GPa), and highest phonon frequencies (in meV) at high-symmetry points in diamond. Experimental values [35–37] are listed for comparison. For the lattice constant and bulk modulus the deviation from the experimental value is indicated in parentheses.

	$a$	$B$	$\omega(\Gamma)$	$\omega(X)$	$\omega(L)$
PBE	3.574 (+0.20%)	430 (−0.19%)	160.5	147.6	154.2
HSE	3.548 (−0.53%)	470 (+0.61%)	169.9	155.1	161.1
expt.	3.567 <sup>a</sup>	443 <sup>b</sup>	166.7 <sup>c</sup>	149.2 <sup>b</sup>	153.0 <sup>b</sup>

<sup>a</sup> Reference 35

<sup>b</sup> Reference 36

<sup>c</sup> Reference 37

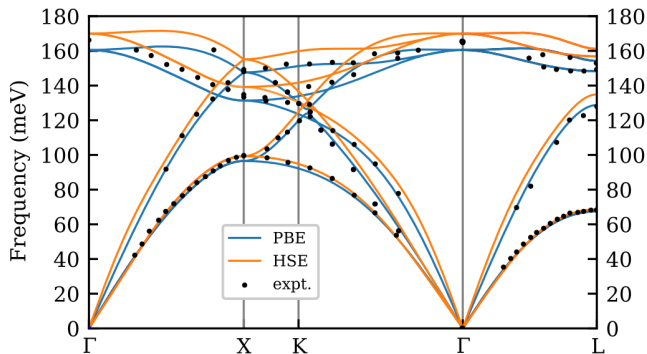


FIG. 2. Phonon dispersion curves of diamond calculated using PBE (blue lines) and HSE (red lines) functionals. Experimental values are taken from Ref. 37.

calculations at the PBE level. We used the projector-augmented wave approach with a plane-wave energy cut-off of 500 eV. Other computational details are given when describing specific systems. Calculations have been performed with the Vienna Ab-initio Simulation Package (VASP) [34].

### A. Bulk parameters and lattice vibrations

Lattice relaxation was performed using a conventional cubic cell with eight carbon atoms. The Brillouin zone was sampled using the Monkhorst-Pack [5]  $8 \times 8 \times 8$   $k$ -point mesh. Results are summarized in Table I. We observe that PBE provides a better description of the lattice constant and the bulk modulus. However, the band gap is significantly underestimated in PBE ( $E_g = 4.12$  eV, compared to the experimental value of 5.48 eV [35]). The band gap is much closer to experiment in HSE ( $E_g = 5.36$  eV).

Phonon dispersion curves were calculated using the PHONOPY software package [38]. Force constants were computed in  $4 \times 4 \times 4$  supercells (containing 512 atoms) using finite displacements and a single  $k$ -point (at  $\Gamma$ ) for

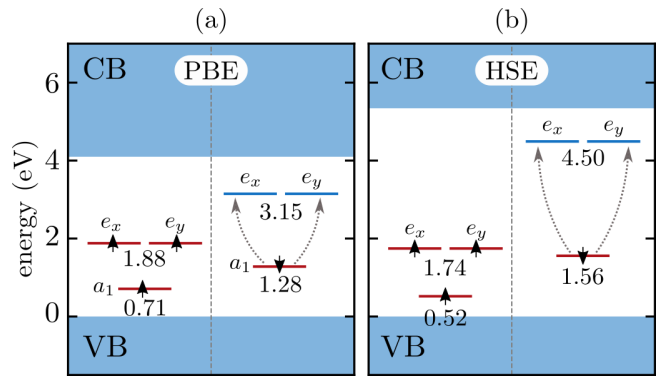


FIG. 3. Defect-level diagrams of the  $\text{NV}^{-1}$  center calculated using PBE (a) and HSE (b) functionals. Diagrams show Kohn-Sham single particle defect levels for the ground state  $^3A_2$ . The spin-majority channel is denoted with upward arrows and the spin-minority channel with downward arrows. Shaded areas correspond to the valence band (VB) and the conduction band (CB). Dotted arrows show optical excitation.

the Brillouin-zone sampling. We have used displacements  $\Delta = 0.01$  Å. In Fig. 2 the calculated phonon dispersion curves are compared with inelastic neutron scattering data from Ref. 37. Our calculations represent phonon dispersion for  $T = 0$ , while experiments have been performed at room temperature. However, due to the very rigid nature of the diamond lattice the phonon frequencies in diamond change by less than 0.1 meV from cryogenic temperatures to room temperature [39], justifying the comparison of calculations with room-temperature data. Our calculations are in full agreement with those of Ref. 33. Both PBE and HSE functionals describe the phonon dispersion reasonably well. However, PBE provides a slightly more accurate description of the spectrum, *e.g.*, for longitudinal acoustic phonons or optical phonons along the paths XK, K $\Gamma$ ,  $\Gamma$ L (Fig. 2). The highest phonon frequencies for high-symmetry points are compared with experiment in Table I.

### B. Negatively charged NV center

In this Section we discuss calculations of the NV center and analyze the convergence of these calculations with respect to the supercell size. We also present the calculations of the vibrational properties of the NV center.

#### 1. Ground state

First-principles calculations of the ground and the excited state of the NV center have been reported previously (for a review see Ref. 40). Here we give an overview of our calculations for completeness. The NV center possesses a  $C_{3v}$  point symmetry and has a stable paramagnetic ground state  $^3A_2$  with spin  $S = 1$ .

Calculated Kohn–Sham defect level diagrams are shown in Fig. 3 for both functionals. In these calculations the defect supercell is a  $4 \times 4 \times 4$  cell with 512 atomic sites. We used a single  $k$ -point (at  $\Gamma$ ) for Brillouin-zone sampling. Theoretical lattice constants were used (Table I) consistently for both functionals. For both spin channels there are three defect levels in the band gap: a fully symmetric  $a_1$  level and a doubly-degenerate  $e$  level. All the levels are filled in the spin-majority channel, and only the  $a_1$  level is filled in the spin-minority channel [10]. The splitting between the two sets of levels is larger in HSE: in the spin-minority channel the difference between the  $a_1$  level and the  $e$  levels is 1.87 eV for PBE and 2.94 eV for HSE. The  ${}^3A_2$  ground state can be described by the electronic configuration  $a_1^2 e^2$ .

## 2. Excited state

The excited state triplet  ${}^3E$  is obtained by promoting the electron in the spin-minority channel from the  $a_1$  level to the  $e$  level (as shown by dashed arrows in Fig. 3), resulting in the electronic configuration  $a_1 e^3$ . We treat the electronic structure of the excited state using the  $\Delta$ SCF method [41], whereby the state is modeled by constraining appropriate Kohn–Sham orbital occupations. The  $\Delta$ SCF method is originally due to Slater, who applied it to optical excitation in atoms; the method was first applied to the NV center by Gali *et al.* [32]

The  ${}^3E$  state is a  $E \otimes e$  Jahn–Teller (JT) system [11, 42] (more precisely, it is a  $E \otimes (e \oplus e \cdots)$  system). The reason for the Jahn–Teller instability is the degeneracy of nominal  $a_1 e_x^2 e_y^1$  and  $a_1 e_x^1 e_y^2$  configurations of the  ${}^3E$  manifold. The  ${}^3E$  state is unstable with respect to symmetry breaking due to the interaction with  $e$  phonons, leading to the lowering of the energy. The Jahn–Teller effect is *dynamical* [11, 42], which qualitatively means that on average the NV center still retains  $C_{3v}$  symmetry. I.e., the adiabatic potential energy surface has a minimum off the high-symmetry point, but the total wavefunction of the ground vibronic level is totally symmetric. The fundamental consequence of the dynamical nature is that wavefunctions that describe the entire system of ions and electrons cannot be factorized into the ionic part and the electronic part. This is already expressed by Eqs. (7) and (8). A more rigorous discussion of the dynamical vs. the static JT effect can be found in Ref. 29.

Vibrational modes obtained in the JT-distorted geometry are inconvenient for theoretical analysis because they lack symmetry properties of the  $C_{3v}$  point group. The existing understanding of the Jahn–Teller effect relies on the use of vibrational modes that have the symmetry of the system in the undistorted configuration,  $C_{3v}$  in our case [29]. Unfortunately, calculations of vibrational frequencies in  $C_{3v}$  symmetry for degenerate states with configurations  $a_1 e_x^2 e_y^1$  or  $a_1 e_x^1 e_y^2$  pose computational difficulties due to the degeneracy of these states. A correct way to proceed would be to perform vibrational analy-

TABLE II. Convergence of the energy difference between the equilibrium configurations  $E'_0$ , as well as lattice relaxation energies  $\Delta E'_g$  and  $\Delta E'_e$  as a function of the supercell size (in eV). Values correspond to the PBE functional and the symmetric electron configuration  $a_1 e_x^{1.5} e_y^{1.5}$  in the excited state.

	$3 \times 3 \times 3$	$4 \times 4 \times 4$	$5 \times 5 \times 5$
$E'_0$	1.719	1.694	1.689
$\Delta E'_g$	0.155	0.173	0.174
$\Delta E'_e$	0.185	0.199	0.205

sis for a mixed electronic state, the density of which is the average of charge densities of the  $a_1 e_x^2 e_y^1$  and  $a_1 e_x^1 e_y^2$  configurations. One can expect that the charge density of such a mixed state would be well approximated with a system with a configuration  $a_1 e_x^{1.5} e_y^{1.5}$ , whereby the electron in the spin-minority channel is split between  $e_x$  and  $e_y$  levels. It is this state with fractional occupations that is used here for the calculation of vibrational properties in the excited state. From now on, the equilibrium geometry of the excited state with the electronic occupations  $a_1 e_x^{1.5} e_y^{1.5}$  will be called a symmetric excited-state configuration (it retains the  $C_{3v}$  symmetry). The equilibrium geometry with electronic occupations  $a_1 e_x^2 e_y^1$  or  $a_1 e_x^1 e_y^2$  will be called an asymmetric excited-state configuration. The asymmetric configuration corresponds to a true physical minimum on the adiabatic excited-state potential energy surface.

## 3. Optical excitation energies

We first test the convergence of calculated energy differences between the ground and excited states  $E_0$ , as well as lattice relaxation energies  $\Delta E_e$  and  $\Delta E_g$  [Fig. 1(c)] as a function of the supercell size. In these calculations the excited state wavefunction and geometry corresponds to the symmetric electron configuration  $a_1 e_x^{1.5} e_y^{1.5}$ . We note that the energy of the system with this electron configuration is not strictly physical due to Coulomb repulsion between a “split” electron occupying two different levels. To emphasize this fact we add a “prime” to energies calculated with this occupation ( $E'_0$ ,  $\Delta E'_e$ ,  $\Delta E'_g$ ). These calculations serve as a numerical test regarding convergence of calculated energies as a function of the supercell size, as they are faster than the calculation with the actual asymmetric configuration  $a_1 e_x^2 e_y^1$  or  $a_1 e_x^1 e_y^2$ . For the same reason we employ the PBE functional in these tests. Results for supercells  $3 \times 3 \times 3$  (216 atomic sites),  $4 \times 4 \times 4$  (512 sites), and  $5 \times 5 \times 5$  (1000 sites) are shown in Table II. The Brillouin zone was sampled at the  $\Gamma$  point. From the results we see that the  $4 \times 4 \times 4$  supercell is sufficient to describe energies with an accuracy of 0.01 eV.

In Table III the calculations of  $E_0$ ,  $\Delta E_g$ , and  $\Delta E_e$  with PBE and HSE functionals are summarized. Values correspond to the physical (asymmetric) electron configura-

TABLE III. Calculated  $E_0$  and relaxation energies for the PBE and HSE functionals (in eV). Values correspond to the electronic configuration  $a_1^1 e^3$  in the excited state and the  $4 \times 4 \times 4$  supercell. In parentheses  $a_1$  and  $e$  components of Franck–Condon shifts are given.

	PBE	HSE
$E_0$	1.689	1.995
$\Delta E_g (a_1 + e)$	0.196 (0.159 + 0.037)	0.257 (0.214 + 0.043)
$\Delta E_e (a_1 + e)$	0.218 (0.182 + 0.036)	0.298 (0.256 + 0.042)

tion  $a_1^1 e^3$  in the excited state and pertain to the  $4 \times 4 \times 4$  supercell. Franck–Condon shifts  $\Delta E_g$  and  $\Delta E_e$  occur due to lattice relaxation which, as discussed in Sec. III has  $a_1$  and  $e$  components. These two contributions are also presented. In short, in the case of  $a_1$  modes this is given by  $\sum_k S_k \hbar \omega_k$ ; in the case of  $e$  modes this is given by  $\sum_k K_k^2 \hbar \omega_k$  (see Secs. VI and VII for the definition of the quantities  $S_k$  and  $K_k^2$ ). We note that the  $e$  component of  $\Delta E_e$  is exactly the Jahn–Teller relaxation energy, often labelled  $E_{JT}$ . The value of  $E_0$  calculated in HSE, 1.995 eV, is close to the experimental ZPL of 1.945 eV. Note that in order to determine the theoretical value of the ZPL we would need to add the contributions of zero-point vibrations  $\varepsilon_{e0} - \varepsilon_{g0}$  as per Eq. (1). Typically this contribution is of the order of  $\sim 10$  meV [43]. We can conclude that the HSE functional provides a very good description of optical excitation energies.

#### 4. Vibrational properties

Here, we define all the quantities needed in the calculation of vibrational properties explicitly; they will be needed in describing the embedding procedure in Sec. V. Central parameters in these calculations are the Hessian matrix elements:

$$\Phi_{\alpha,\beta}(m,n) = \frac{\partial F_{m,\alpha}}{\partial r_{n,\beta}}, \quad (19)$$

where  $F_{m,\alpha}$  is the force that acts on atom  $m$  in the Cartesian direction  $\alpha$  and  $r_{n,\beta}$  is the displacement of atom  $n$  from equilibrium in the direction  $\beta$ . The Hessian matrix of the NV center is calculated using the finite-difference approach [44]. This requires a large number of SCF calculations; however, this number can be reduced employing symmetry properties. The dynamical matrix element is defined as  $D_{\alpha,\beta}(m,n) = \Phi_{\alpha,\beta}(m,n)/\sqrt{M_\alpha M_\beta}$ , where  $M_\alpha$  and  $M_\beta$  are atomic masses. Diagonalization of the dynamical matrix yields mass-weighted normal modes  $\eta_k$  and vibrational frequencies  $\omega_k$  of the defect. We then classify the obtained modes according to the irreducible representation of the  $C_{3v}$  group, *i.e.*,  $a_1$ ,  $a_2$ , or  $e$ . Actual calculations of dynamical matrix elements were performed in  $4 \times 4 \times 4$  supercells for both PBE and HSE.

## V. EMBEDDING METHODOLOGY

In Sec. IV B 2 we showed that the parameters of the configuration coordinate diagram related to the optical excitation of the NV center are converged within 0.01 eV in the  $4 \times 4 \times 4$  supercell. However, while such supercells allow calculating the general features of the optical lineshapes, they are not sufficient if our goal is to obtain lineshapes with high accuracy and high energy resolution [8].

Let us take the  $4 \times 4 \times 4$  supercell as an example. As will be explained in Secs. VI and VII, optical lineshapes reflect lattice relaxation at the defect caused by the optical transition. In essence, optical spectra reflect the decomposition of these relaxations in the basis of vibrational modes. The lowest-frequency mode at the  $\Gamma$  point in the  $4 \times 4 \times 4$  supercell is 35.0 meV for the NV center in the ground state (PBE result). The resulting calculations of optical lineshapes can therefore not contain any contributions of modes with lower frequencies. In contrast, the experimental luminescence lineshape clearly shows the contribution of all acoustic phonons down to zero frequencies [45]. Because the relaxations have the periodicity of the lattice the problem is not resolved by calculating the phonon spectrum in the entire Brillouin zone of the supercell, as only  $\Gamma$  phonons contribute (see Sec. VI for a more quantitative discussion).

We solve this issue by the use of the embedding methodology [8], which enables us to compute lattice relaxations and vibrational modes for supercells  $N \times N \times N$  for which direct first-principles calculations are too expensive. We apply the methodology for supercells with  $N \geq 5$ . The idea has two principal components: (i) calculations of lattice relaxations in these large supercells; (ii) calculation of vibrational spectra in these supercells. At the core of our methodology is the fact that interatomic interactions in diamond are short-ranged. The meaning of this statement and the importance for the two aspects mentioned above are as follows: (a) when the electronic structure of the defect changes from  $^3E$  to  $^3A_2$  (or vice versa) for *fixed* lattice positions, the forces that appear on the atoms surrounding the defect decay fast as a function of the distance from the defect; and (b) when the position of one atom changes in a fixed electronic state, the induced force on neighboring atoms also decays very fast as a function of a distance from this atom. Property (a) enables us to calculate lattice relaxations in very large supercells. A quantitative description will be given in Secs. VI and VII. Property (b) enables the construction of the Hessian matrix, and therefore the study of vibrational modes of NV centers embedded in these large supercells. The remainder of this Section is devoted to the explanation of the second component of our methodology.

The Hessian matrix  $\Phi_{\alpha,\beta}(m,n)$  [Eq. (19)] of a large defect supercell is constructed as follows. If atoms  $n$  and  $m$  are separated by a distance larger than a chosen cutoff radius  $r_{c1}$ , then the Hessian matrix element is set to zero.

If both atoms are separated from either the nitrogen atom or the vacant site by a distance smaller than the cutoff radius  $r_{c2}$ , then we use the Hessian matrix element from the actual defect supercell. For all other atom pairs we use bulk values.

While the procedure is straightforward, it requires some corrections. Setting matrix elements beyond a certain radius to zero can break Newton's third law

$$\Phi_{\alpha,\beta}(n,n) = - \sum_{m \neq n} \Phi_{\alpha,\beta}(m,n). \quad (20)$$

Breaking this ‘‘acoustic sum rule’’ would introduce a small but nonzero net force on the entire system that could affect the results for low-frequency acoustic modes. We could enforce the fulfillment of Newton's third law by setting each matrix element  $\Phi_{\alpha,\beta}(n,n)$  (diagonal in the atomic index  $n$ ) equal to the rhs of Eq. (20). However, such a correction for  $\alpha \neq \beta$  can break the symmetry of the Hessian matrix:

$$\Phi_{\alpha,\beta}(n,n) = \Phi_{\beta,\alpha}(n,n), \quad (21)$$

which follows from a more general symmetry property:  $\Phi_{\alpha,\beta}(m,n) = \Phi_{\beta,\alpha}(n,m)$ . To ensure that (i) the frequency of acoustic modes at the  $\Gamma$  point is equal to 0 and (ii) symmetry properties of the Hessian are preserved we set  $\Phi_{\alpha,\beta}(n,n)$  to the rhs of (20) only in the case when  $\alpha = \beta$ .

Regarding the parameter  $r_{c1}$  in the embedding procedure, we used the value  $r_{c1} = 7$  Å. In the case of  $r_{c2}$  we used a slightly smaller value,  $r_{c2} = 5.6$  Å, to reduce the overall computational cost in hybrid functional calculations. We expect the error bar of the embedding procedure to be  $\sim 2$  meV, obtained from the convergence tests of bulk phonons (see, e.g., Ref. 43).

The embedding procedure was applied to supercells up to  $N = 20$ . A  $N \times N \times N$  supercell contains  $8N^3$  atomic sites, and thus  $24N^3$  degrees of freedom. Thus, to find vibrational modes and frequencies we need to diagonalize dynamical matrices as large as  $192\,000 \times 192\,000$ . Since these matrices are sparse, with only  $\sim 0.5\%$  of nonzero elements (sparsity 99.5%), we used the spectrum slicing technique [46] based on the shift-and-invert Lanczos method, as implemented in the SLEPc [47] library. Parallelization was done using an interface to the MUMPS [48] parallel sparse direct solver.

## VI. COUPLING TO $A_1$ MODES

### A. General formulation

In this Section we discuss the calculation of spectral functions  $A_{a_1}(\hbar\omega)$ , as defined in Eqs. (13) and (15). The calculation of these spectral functions is difficult for two main reasons. The first reason is that the evaluation of overlap integrals  $\langle \chi_{e0}^{a_1} | \chi_{gp}^{a_1} \rangle$  or  $\langle \chi_{es}^{a_1} | \chi_{g0}^{a_1} \rangle$  entering equations (13) and (15) is computationally very challenging,

since, generally speaking, normal modes in the ground and the excited state will not be identical. The two sets of modes are related via the so-called Duschinsky transformation [3]. Because the vibrational modes in the ground and the excited state differ, as explicitly confirmed by our calculations, overlap integrals are highly multidimensional integrals. To overcome this problem we will assume the *equal-mode approximation*, as is nearly always done for solid-state systems [2].

We will describe the geometry of the entire system using normal coordinates  $Q_k$ , i.e. Cartesian coordinates projected on normal modes  $\boldsymbol{\eta}_k$ :

$$Q_k = \sum_{\alpha} \sqrt{M_{\alpha}} (\mathbf{R}_{\alpha} - \mathbf{R}_{g,\alpha}) \boldsymbol{\eta}_{k;\alpha}, \quad (22)$$

where  $\mathbf{R}_{\alpha}$  is the position of atom  $\alpha$ ,  $\mathbf{R}_{g,\alpha}$  is its equilibrium position in the ground state,  $M_{\alpha}$  is the mass of atom  $\alpha$ , and  $\boldsymbol{\eta}_{k;\alpha}$  is a vector that describes the three components of the mode  $\boldsymbol{\eta}_k$  for atom  $\alpha$ . Within the equal-mode approximation the change of the adiabatic potential energy surface as a result of optical excitation is linear in normal coordinates:

$$\Delta V(\mathbf{Q}) = V_e(\mathbf{Q}) - V_g(\mathbf{Q}) = \sum_k q_k Q_k, \quad (23)$$

where  $q_k$  are linear coupling constants. In the expression above we omit a constant energy offset that does not affect overlap integrals. In this approximation vibrational modes and frequencies in the ground and the excited state are identical, but the harmonic potential describing each vibrational mode  $k$  is displaced by  $\Delta Q_k = q_k / \omega_k^2$  [19],  $\omega_k$  being the angular frequency of the mode  $k$ .

The overlap integral of two same-frequency displaced harmonic-oscillator wavefunctions, pertaining to the vibrational mode  $k$ , has an elegant analytical expression [19]:

$$|\langle \chi_0^k(Q) | \chi_n^k(Q - \Delta Q_k) \rangle|^2 = \frac{S_k^n}{n!} \exp(-S_k) \quad (24)$$

where

$$S_k = \frac{\omega_k \Delta Q_k^2}{2\hbar} \quad (25)$$

is the partial Huang–Rhys (HR) factor. This factor has a statistical interpretation as the average number of  $k$ -mode phonons created during an optical transition [1]. Partial Huang–Rhys factors define the so-called spectral density of electron–phonon coupling  $S(\hbar\omega)$ , which is the key property that needs to be computed in order to calculate  $A_{a_1}(\hbar\omega)$ :

$$S_{a_1}(\hbar\omega) = \sum_k S_k \delta(\hbar\omega - \hbar\omega_k). \quad (26)$$

The total Huang–Rhys factor due to coupling to  $a_1$  modes is then

$$S_{a_1} = \int_0^{\infty} S_{a_1}(\hbar\omega) d(\hbar\omega) = \sum_k S_k. \quad (27)$$



As seen in the expressions above, we use similar notation for  $S_{a_1}$ , the total Huang–Rhys factor and a dimensionless quantity, and  $S_{a_1}(\hbar\omega)$ , a spectral density with units [1/energy]. However, this should cause no confusion, as the spectral density can always be identified based on the indicated functional dependence on  $\hbar\omega$ .

Evaluation of spectral functions (13) and (15) is simplified if one considers their Fourier transform to the time domain, commonly denoted as the *generating function* [27]:

$$G(t) = \int A_{a_1}(\hbar\omega) e^{i\omega t} d(\hbar\omega). \quad (28)$$

The generating function for luminescence is given by

$$G(t) = \exp \left[ -iE_{\text{ZPL}}t/\hbar - S_{a_1} + \int e^{i\omega t} S_{a_1}(\hbar\omega) d(\hbar\omega) \right], \quad (29)$$

and similarly for absorption [49]:

$$G(t) = \exp \left[ -iE_{\text{ZPL}}t/\hbar - S_{a_1} + \int e^{-i\omega t} S_{a_1}(\hbar\omega) d(\hbar\omega) \right]. \quad (30)$$

Once generating functions are known, spectral functions can be obtained via the inverse Fourier transform:

$$A_{a_1}(\hbar\omega) = \frac{1}{2\pi} \int_{-\infty}^{\infty} e^{i\omega t} G(t) e^{-\gamma|t|} dt \quad (31)$$

The term  $e^{-\gamma|t|}$  is included to account for the homogeneous broadening of the optical transition.

The main task is therefore the calculation of partial Huang–Rhys factors  $S_k$  via Eq. (25). The coefficients  $\Delta Q_k$  in that equation describe the change of the equilibrium defect geometry upon optical transition and are given by to the equation similar to Eq. (22):

$$\Delta Q_k = \sum_{\alpha} \sqrt{M_{\alpha}} \Delta \mathbf{R}_{\alpha} \boldsymbol{\eta}_{k;\alpha}. \quad (32)$$

Here  $\Delta \mathbf{R}_{\alpha} = \mathbf{R}_{e,\alpha} - \mathbf{R}_{g,\alpha}$  is the change of the equilibrium position of atom  $\alpha$  between the ground and the excited state.

As discussed in Sec. V, actual geometry relaxations  $\Delta \mathbf{R}_{\alpha}$  extend much farther than can be described using moderate-size supercells used in first-principles calculations. To address this problem we note that within the harmonic approximation  $\Delta Q_k$  can alternatively be expressed as

$$\Delta Q_k = \frac{1}{\omega_k^2} \sum_{\alpha} \frac{\mathbf{F}_{\alpha}}{\sqrt{M_{\alpha}}} \boldsymbol{\eta}_{k;\alpha}, \quad (33)$$

where  $\mathbf{F}_{\alpha}$  is the force on atom  $\alpha$  induced by the electronic transition. Specifically, in the case of luminescence this is the force in the equilibrium geometry of the excited state when the wavefunction is that of the ground state [point *B* in Fig. 1(c)]. In the case of absorption it is the force in the equilibrium geometry of the ground

state when the wavefunction is that of the excited state [point *D* in Fig. 1(c)]. In the case of elastic interactions, as is the case for the NV centre in diamond,  $\mathbf{F}_{\alpha}$  decays much more rapidly with distance from the defect center compared to  $\Delta \mathbf{R}_{\alpha}$ . Indeed, when the electronic state is changed, only atoms in the immediate surrounding experience the change in the force. However, once those atoms start to move under the influence of these forces, the resulting displacements  $\Delta \mathbf{R}_{\alpha}$  are long-ranged (see also Appendix B of Ref. 8).

We tested that contributions to the spectral density of electron–phonon coupling  $S_{a_1}(\hbar\omega)$  are already converged if we ignore the forces for atoms lying further than than  $r_{c1} = 7$  Å from the nitrogen site. Because of this rapid decay of forces, shown in Sec. I of the Supplemental Material [50], we make an approximation that the same forces would be obtained in larger supercells that are not amenable to explicit first-principles calculations. This constitutes aspect (i) of the embedding methodology discussed in Sec. V.

Equations (25), (26), and (33) define the procedure for the calculation of  $S_{a_1}(\hbar\omega)$  within the equal-mode approximation. However, since vibrational modes in the ground and the excited state *are* different, one has to choose which vibrational modes to use in the calculation. In Sec. II of the Supplemental Material we show, by means of a simplified model, that in the case of luminescence it is best to choose vibrational modes and frequencies of the ground state, while in the case of absorption it is best to choose those of the excited state. This is the choice we will be making for all the results reported in this paper.

## B. Results: luminescence

Figure 4 shows how the spectral density due to the coupling to  $a_1$  phonons [Eq. (26)] converges as a function of the supercell size. The results pertain to the PBE functional, and  $\delta$ -functions in Eq. (26) have been replaced by Gaussians. In order to obtain a smooth function throughout the whole vibrational spectrum we have used Gaussians of variable width. Our tests indicated that choosing  $\sigma$  to vary linearly from  $\sigma = 3.5$  meV for  $\omega = 0$  to  $\sigma = 1.5$  meV for the highest-energy phonon results in a smooth spectral density without introduction of any artifacts. This smearing procedure will be used for all spectral densities in this paper.

Figure 4 shows that for phonon frequencies  $> 100$  meV the spectral density is already converged for supercells  $12 \times 12 \times 12$  or even  $8 \times 8 \times 8$  (inset). However, larger supercells are needed to converge  $S_{a_1}(\hbar\omega)$  for energies  $< 60$  meV. The essence of our embedding procedure discussed in Sec. V was exactly to achieve this smooth behavior throughout the whole phonon spectrum. It is also because of a slower convergence in the low-frequency part of the spectrum that the smearing procedure with a varying  $\sigma$  was used.

PBE and HSE spectral densities for the  $20 \times 20 \times 20$  su-

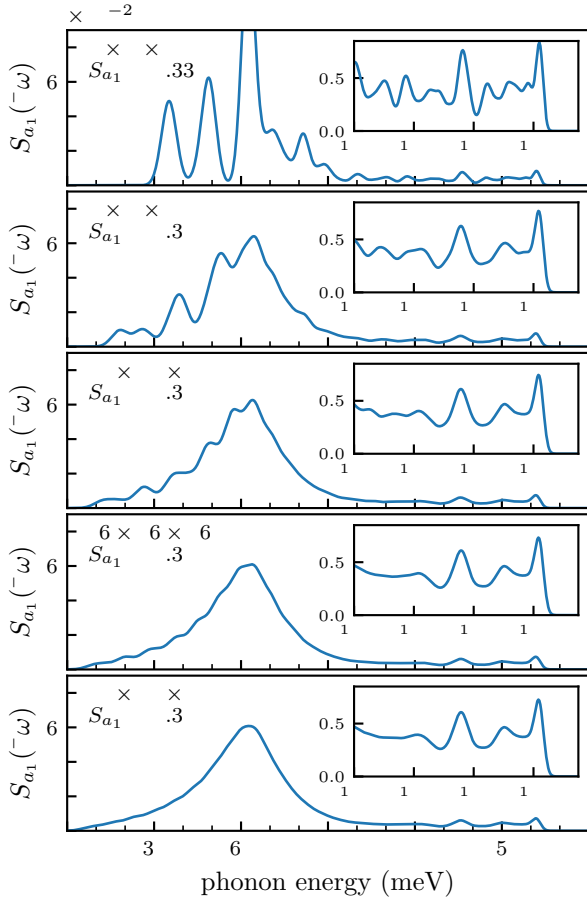


FIG. 4. Convergence of spectral densities  $S_{a_1}(\hbar\omega)$  (in units 1/meV) due to coupling to  $a_1$  phonons with respect to the supercell size. Supercells range in size from  $4 \times 4 \times 4$  (512 atomic sites) to  $20 \times 20 \times 20$  (64 000 sites). Huang–Rhys factors for each supercell are also given. The insets enlarge the high-frequency part. Gaussian smearing with varying  $\sigma$  was used, as explained in the text.

percells are compared in Fig. 5(a). HSE yields noticeably stronger electron–phonon interactions with the total HR factor being  $\sim 33\%$  larger. The most pronounced features in the HSE spectral density are shifted to slightly higher phonon energies. For example, the ratios  $\omega_{\text{HSE}}/\omega_{\text{PBE}}$  for the three most-pronounced peaks in the PBE spectrum, at 62.5, 135.7 and 161.6 meV, are 1.054, 1.057 and 1.051. This difference stems from the fact that the bonds are stiffer in HSE in comparison to PBE, as reflected in the difference of lattice constants. In fact, these ratios are very similar to the ones for bulk phonons given in Table I. Apart from this, the shapes of the two spectral densities are rather similar.

Calculated spectral functions  $A_{a_1}(\hbar\omega)$  [Eq. (13)] for the two functionals are shown in Fig. 5(b). These functions were calculated using Eq. (29) and  $\gamma = 0.3$  meV in Eq. (31). Since the actual luminescence line contains contributions from both  $a_1$  and  $e$  phonons, we leave the comparison with experiment to Sec. VIII.

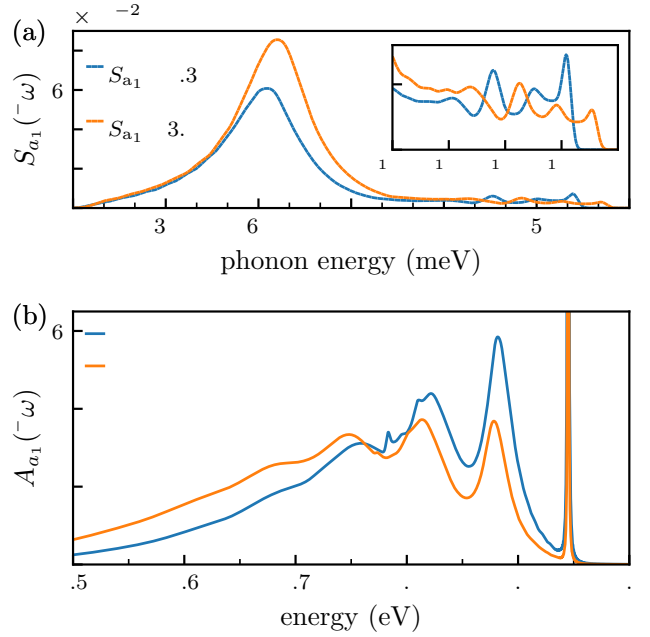


FIG. 5. (a) Spectral densities  $S_{a_1}(\hbar\omega)$  (in units 1/meV) due to coupling to  $a_1$  phonons for luminescence, calculated with PBE and HSE functionals. Huang–Rhys factors are also given. The inset enlarges the high-frequency part. (b) Spectral functions  $A_{a_1}(\hbar\omega)$  [in units 1/eV, Eq. (13)] for luminescence calculated using PBE and HSE. The ZPL energy is set to the experimental value.

### C. Results: absorption

To calculate  $S_{a_1}(\hbar\omega)$  for absorption one needs to calculate forces in the excited state  $\mathbf{F}_\alpha$  at the geometry of the ground state [point D in Fig. 1(c)], where the two  $^3E$  states are degenerate.

Due to issues related to the convergence of the electronic structure for the degenerate state, we calculate these forces indirectly from displacements via:

$$\mathbf{F}_\alpha = \sqrt{M_\alpha} \sum_k \omega_k^2 \boldsymbol{\eta}_{k;\alpha} \Delta Q_k, \quad (34)$$

where  $\omega_k$  and  $\boldsymbol{\eta}_{k;\alpha}$  are calculated in the  $4 \times 4 \times 4$  supercell, and  $\Delta Q_k$  are given by Eq. (32). At a first glance, the procedure to calculate the displacements might appear circular. This is not the case. We use the calculated displacements in the  $4 \times 4 \times 4$  supercell to “restore” the forces in this supercell. These forces are then used to determine the displacements in large supercells for which actual first-principles calculations are not possible.

Spectral densities  $S_{a_1}(\hbar\omega)$  for absorption in the case of the  $20 \times 20 \times 20$  supercell are shown in Fig. 6 (a). Compared to emission, one sees slightly larger differences between the shapes of spectral densities calculated in PBE and HSE. PBE calculations exhibit a broad peak at  $\sim 60$  meV and this peaks shifts to  $\sim 75$  meV in HSE. Spectral functions  $A_{a_1}(\hbar\omega)$  for absorption [Eq. (15)] for the two functionals are shown in Fig. 6 (b). As in the

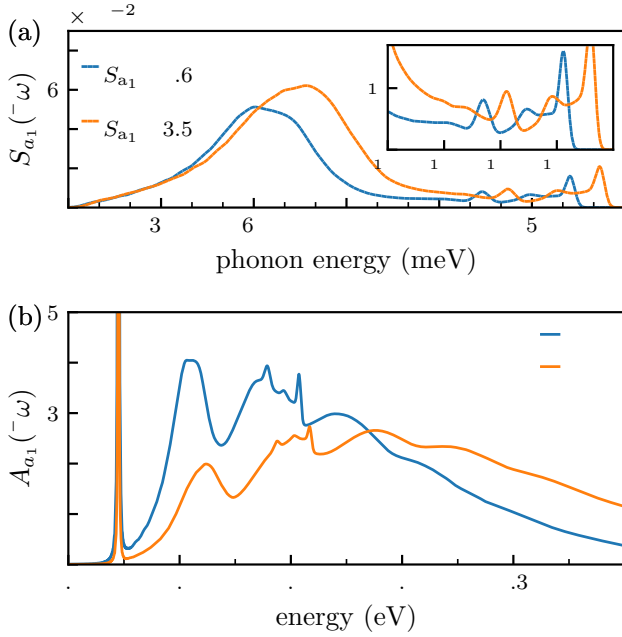


FIG. 6. (a) Spectral densities  $S_{a_1}(\hbar\omega)$  (in units 1/meV) due to coupling to  $a_1$  phonons for absorption, calculated with PBE and HSE functionals. Huang-Rhys factors are also given. The inset enlarges the high-frequency part. (b) Spectral functions  $A_{a_1}(\hbar\omega)$  [in units 1/eV, Eq. (15)] for absorption calculated using PBE and HSE. The ZPL energy is set to the experimental value.

case of luminescence, the comparison to experiment is left for Sec. VIII.

## VII. COUPLING TO $E$ VIBRATIONS: MULTI-MODE JAHN-TELLER PROBLEM

The coupling to  $e$  modes during optical transitions occurs because of the JT effect in the  ${}^3E$  state. As discussed in Sec. IV B 2, the effect is dynamical. [19] The dynamical nature of the effect has been confirmed by the  $\sim T^5$  broadening of the ZPL at low temperatures, [11] as well as by actual calculations of the potential energy surface. [42]

The purpose of the present Section is to calculate spectral functions of coupling to  $e$  vibrations, given by Eqs. (14) and (16).

### A. Multi-mode Jahn-Teller effect: general theory and the choice of basis

The dynamical JT effect is described in a number of articles and books, e.g., Refs. 19, 29, and 51. Here we briefly review the general theory of this effect, and derive the expressions that are used in our calculations.

The vibronic wavefunction of the excited state is given in Eq. (9).  $a_1$ -symmetry vibrational wavefunctions  $\chi_{es}^{a_1}(\mathbf{Q}_{a_1})$  were addressed in Sec. VI. The  $e$ -symmetry

part  $|\Phi_{et}\rangle = \chi_{et}^{e_x}(\mathbf{Q}_e)|E_x\rangle + \chi_{et}^{e_y}(\mathbf{Q}_e)|E_y\rangle$  [Eq. (8)] can be represented in the  $\{|E_x\rangle, |E_y\rangle\}$  basis as a two-component vector  $(\chi_{et}^{e_x}, \chi_{et}^{e_y})$ . In this representation  $|\Phi_{et}\rangle$  is an eigenvector of the vibronic Hamiltonian [29]:

$$\hat{\mathcal{H}} = \hat{\mathcal{H}}_0 + \hat{\mathcal{H}}_{\text{JT}}. \quad (35)$$

Here

$$\hat{\mathcal{H}}_0 = \hat{C}_z \sum_{k;\gamma \in x,y} \left( -\frac{\hbar^2}{2} \frac{\partial^2}{\partial Q_{k\gamma}^2} + \frac{1}{2} \omega_k^2 Q_{k\gamma}^2 \right) \quad (36)$$

describes the motion in the harmonic potential, while

$$\hat{\mathcal{H}}_{\text{JT}} = \sum_{k;\gamma \in x,y} \hat{C}_\gamma V_k Q_{k\gamma} \quad (37)$$

is the linear Jahn-Teller interaction.  $\omega_k$  are angular frequencies of vibrations,  $V_k$  are vibronic coupling coefficients, and  $k = 1 \dots N$  runs over all pairs of degenerate  $e$ -symmetry vibrations. In the expressions above  $\hat{C}_\gamma$  are matrices [20]:

$$\hat{C}_x = \begin{pmatrix} 0 & 1 \\ 1 & 0 \end{pmatrix}, \quad \hat{C}_y = \begin{pmatrix} 1 & 0 \\ 0 & -1 \end{pmatrix}, \quad \hat{C}_z = \begin{pmatrix} 1 & 0 \\ 0 & 1 \end{pmatrix}.$$

The Schrödinger equation  $\hat{\mathcal{H}}|\Phi_{et}\rangle = \varepsilon_{et}|\Phi_{et}\rangle$  can be solved by diagonalizing the Hamiltonian in the basis of eigenvectors of  $\hat{\mathcal{H}}_0$  [29]. One of the obvious choices for this basis are wavefunctions of the type  $|n_{1x}n_{1y} \dots n_{Nx}n_{Ny}; E_x\rangle$  and  $|n_{1x}n_{1y} \dots n_{Nx}n_{Ny}; E_y\rangle$ .  $n_{kx}$  and  $n_{ky}$  are vibrational quantum numbers pertaining to the doubly-degenerate mode  $k$ . However, this choice of the basis is not the most convenient when dealing with many  $e$  modes. A more convenient choice is provided by so called “chiral” phonons, as explained in the following.

As a preliminary, let us consider [51] the operator  $\hat{J} = \hat{J}_{\text{el}} + \hat{J}_{\text{ph}}$ , where

$$\hat{J}_{\text{el}} = \frac{\hbar}{2} \hat{\sigma}_y, \quad \hat{J}_{\text{ph}} = \hat{C}_z \sum_k \hat{L}_{z,k}. \quad (38)$$

Here  $\hat{J}_{\text{ph}}$  is the sum of phonon angular momentum operators  $\hat{L}_{z,k} = i\hbar (Q_{kx} \partial / \partial Q_{ky} - Q_{ky} \partial / \partial Q_{kx})$  that acts in a two-dimensional subspace of normal modes  $\{Q_{kx}, Q_{ky}\}$ .  $\hat{J}_{\text{el}}$  acts on the orbital part of the wavefunction and  $\hat{\sigma}_y$  is the Pauli matrix.  $\hat{J}$  commutes with both  $\hat{\mathcal{H}}_0$  and  $\hat{\mathcal{H}}_{\text{JT}}$ , and therefore also with  $\hat{\mathcal{H}}$ .

Let us now find wavefunctions that would be eigenstates of  $\hat{\mathcal{H}}_0$ , and simultaneously of  $\hat{J}_{\text{el}}$  and  $\hat{J}_{\text{ph}}$ . The orbital eigenstates of the operator  $\hat{J}_{\text{el}}$  are  $|E_\pm\rangle = 1/\sqrt{2}(|E_x\rangle \pm i|E_y\rangle)$  with eigenvalues  $J_{\text{el}} = \pm \frac{\hbar}{2}$ . Expressing  $J_{\text{el}} = j_{\text{el}}\hbar$  enables us to define a quantum number  $j_{\text{el}} = \pm 1/2$ , usually called the electronic pseudo-spin. Since  $\hat{\mathcal{H}}_0$  does not mix different electronic states,  $|E_\pm\rangle$  [or  $(1/\sqrt{2}, \pm i/\sqrt{2})$  in the assumed matrix notation] are also eigenstates of  $\hat{\mathcal{H}}_0$ .

To find common eigenstates of  $\hat{J}_{\text{ph}}$  and  $\hat{\mathcal{H}}_0$  we will describe the vibrational degrees of freedom by the aforementioned “chiral” phonons. Second-quantization operators of these phonons are [52]:

$$a_{k+} = \frac{1}{\sqrt{2}}(a_{kx} - ia_{ky}), \quad a_{k-} = \frac{1}{\sqrt{2}}(a_{kx} + ia_{ky}),$$

where  $a_{kx}$  and  $a_{ky}$  pertain to normal modes  $Q_{kx}$  and  $Q_{ky}$ , respectively. Defining the number operator of right- and left-hand phonons as  $\hat{n}_{k\pm} = a_{k\pm}^\dagger a_{k\pm}$  we can rewrite the total phonon angular momentum operator as

$$\hat{J}_{\text{ph}} = \hat{C}_z \hbar \sum_k (\hat{n}_{k+} - \hat{n}_{k-}) \quad (39)$$

and  $\hat{\mathcal{H}}_0$  as

$$\hat{\mathcal{H}}_0 = \hat{C}_z \sum_k \hbar \omega_k (\hat{n}_{k+} + \hat{n}_{k-} + 1). \quad (40)$$

By comparing Eqs. (39) and (40) we see that the common eigenfunctions of  $\hat{\mathcal{H}}_0$  and  $\hat{J}_{\text{ph}}$  can be described by two quantum numbers for each pair of  $e$  phonons  $k$ :  $n_k = n_{k+} + n_{k-}$ , the total number of  $k$ -phonons, and  $l_k = n_{k+} - n_{k-}$ , whereby  $L_k = l_k \hbar$  is the angular momentum quantum number associated with  $k$ -phonons. Since  $n_{k+}$  and  $n_{k-}$  are integers, for a given  $n_k$ ,  $l_k$  takes values  $l_k = n_k, n_k - 2, n_k - 4, \dots, -n_k$ .

It follows from the previous discussion that common eigenstates of  $\hat{\mathcal{H}}_0$ ,  $\hat{J}_{\text{el}}$ , and  $\hat{J}_{\text{ph}}$  can be written as  $|n_1 l_1 \dots n_N l_N; E_+\rangle$  and  $|n_1 l_1 \dots n_N l_N; E_-\rangle$ . As they are also eigenfunctions of  $\hat{J} = \hat{J}_{\text{el}} + \hat{J}_{\text{ph}}$ , these wavefunctions can be characterized by a quantum number

$$j = j_{\text{el}} + \sum_k l_k.$$

The new basis functions are eigenfunctions of  $\hat{\mathcal{H}}_0$ , but, certainly, not of  $\hat{\mathcal{H}}_{\text{JT}}$ . If we express  $Q_{k\gamma}$  in the Jahn–Teller Hamiltonian Eq. (37) in terms of creation and annihilation operators  $a_{k\pm}$  and  $a_{k\pm}^\dagger$ , we can rewrite  $\hat{\mathcal{H}}_{\text{JT}}$  as

$$\hat{\mathcal{H}}_{\text{JT}} = \sqrt{2} \sum_k K_k \hbar \omega_k \begin{pmatrix} 0 & a_{k+} + a_{k-}^\dagger \\ a_{k-} + a_{k+}^\dagger & 0 \end{pmatrix}. \quad (41)$$

The parameters  $K_k = V_k / \sqrt{2\hbar\omega_k^3}$  are dimensionless vibronic constants [18]. We can then derive matrix elements of  $\hat{\mathcal{H}}_{\text{JT}}$  in the new basis:

$$\begin{aligned} & \langle n'_1 l'_1, \dots, n'_N l'_N; E_- | \hat{\mathcal{H}}_{\text{JT}} | n_1 l_1, \dots, n_N l_N; E_+ \rangle \\ &= \sqrt{2} \sum_k K_k \hbar \omega_k \delta_{l'_k l_k + 1} \left[ \prod_{j \neq k} \delta_{n'_j n_j} \delta_{l'_j l_j} \right] \\ & \times \left[ \sqrt{\frac{n_k - l_k}{2}} \delta_{n'_k n_k - 1} + \sqrt{\frac{n_k + l_k + 2}{2}} \delta_{n'_k n_k + 1} \right]. \end{aligned} \quad (42)$$

We note that  $\hat{\mathcal{H}}_{\text{JT}}$  couples only electronic states of different electron pseudo-spin.  $\hat{\mathcal{H}}_0$  is diagonal in both vibrational quantum numbers and orbital degrees of freedom with matrix elements:

$$\begin{aligned} & \langle n_1 l_1, \dots, n_N l_N; E_\pm | \hat{\mathcal{H}}_0 | n_1 l_1, \dots, n_N l_N; E_\pm \rangle \\ &= \sum_k \hbar \omega_k (n_k + 1). \end{aligned} \quad (43)$$

Equations (42) and (43) are the final expressions for the vibronic Hamiltonian in the basis of “chiral” phonons.

The logic for choosing the new basis can be recapped as follows.  $\hat{\mathcal{H}}_{\text{JT}}$  and thus  $\hat{\mathcal{H}} = \hat{\mathcal{H}}_0 + \hat{\mathcal{H}}_{\text{JT}}$  do not commute with  $\hat{J}_{\text{el}}$  and  $\hat{J}_{\text{ph}}$  separately. However, as discussed above,  $\hat{\mathcal{H}}$  commutes with  $\hat{J}_{\text{el}} + \hat{J}_{\text{ph}}$ . Therefore the Hamiltonian only couples basis states with the same quantum number  $j$ , thus separating the diagonalization problem for different angular momentum components  $j$  [51]. This is the biggest advantage of the new basis. The procedure for diagonalizing  $\hat{\mathcal{H}} = \hat{\mathcal{H}}_0 + \hat{\mathcal{H}}_{\text{JT}}$  is described in Sec. VIID.

## B. Calculation of coupling parameters

The first task in the solution of the vibronic problem is to calculate linear coupling constants  $V_k$  or, alternatively, dimensionless parameters  $K_k$ . In the case of the JT effect the adiabatic potential energy surface in the subspace  $\{Q_{kx}, Q_{ky}\}$  (a single  $e$  pair) has two branches with energies [29]:

$$U_k(Q_k) = \frac{1}{2} \omega_k^2 Q_k^2 \pm V_k Q_k, \quad (44)$$

where  $Q_k^2 = Q_{kx}^2 + Q_{ky}^2$ . Energy minimization in DFT self-consistent calculations follows the lower-lying branch of Eq. (44). The minimum of this potential occurs at  $\Delta Q_k = V_k / \omega_k^2$ . This enables the determination of  $V_k$  and thus  $K_k$  once  $\Delta Q_k$  is known:

$$K_k^2 = \frac{\omega_k \Delta Q_k^2}{2\hbar}. \quad (45)$$

We find  $\Delta Q_k$  from

$$\Delta Q_k^2 = \Delta Q_{kx}^2 + \Delta Q_{ky}^2, \quad (46)$$

where

$$\Delta Q_{k\gamma} = \frac{1}{\omega_k^2} \sum_\alpha \frac{\mathbf{F}_\alpha}{\sqrt{M_\alpha}} \boldsymbol{\eta}_{k\gamma;\alpha} \quad (47)$$

Here, as above,  $\gamma = \{x, y\}$ . Equation (47) is identical to Eq. (33) (see Sec. VI for the description of parameters), with the only difference that Eq. (47) is applied to  $e$  modes rather than  $a_1$  modes. In the case of absorption forces  $\mathbf{F}_\alpha$  are obtained as in Sec. VIC.

Comparing Eq. (45) with Eq. (25) we see that the dimensionless parameter  $K_k^2$  plays a similar role to the partial Huang–Rhys factor  $S_k$  in the case of coupling to  $a_1$



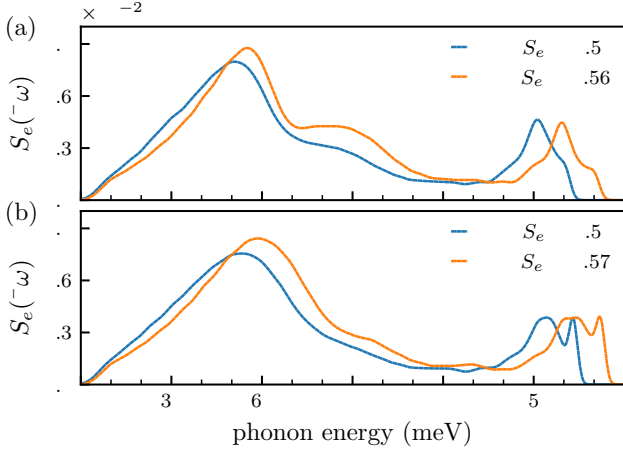


FIG. 7. Spectral density  $S_e(\hbar\omega)$  (in units  $1/\text{meV}$ ) due to coupling to  $e$  phonons for (a) luminescence and (b) absorption, calculated with PBE and HSE functionals. Results are for the  $20 \times 20 \times 20$  supercell. Huang–Rhys factors are also given.

modes. A different notation is used for historical reasons. Thus, in analogy to Eq. (26), we introduce a spectral density of coupling to asymmetric  $e$  modes, given by:

$$S_e(\hbar\omega) = \sum_k K_k^2 \delta(\hbar\omega - \hbar\omega_k),$$

where the sum runs over all  $e$  doublets. As in the case of  $S_{a_1}(\hbar\omega)$ ,  $S_e(\hbar\omega)$  depends on the supercell size, converging towards the final result as the system size increases. The result for the  $20 \times 20 \times 20$  supercell is shown in Fig. 7. The integral of this function quantifies the strength of the Jahn–Teller interaction in a system, which we will label  $S_e$ :

$$S_e = \sum_k K_k^2 = \int_0^\infty S_e(\hbar\omega) d(\hbar\omega). \quad (48)$$

For simplicity of the nomenclature we will also call it a Huang–Rhys factor pertaining to coupling to  $e$  modes. Jahn–Teller interaction is considered strong for  $S_e \gg 1$ , and weak in the case of  $S_e \ll 1$  [29]. For the NV center HSE values are  $S_e = 0.56$  for emission and  $S_e = 0.57$  for absorption. One can conclude that the JT coupling is of medium strength.

### C. Luminescence and absorption processes

Diagonalization of  $\hat{\mathcal{H}} = \hat{\mathcal{H}}_0 + \hat{\mathcal{H}}_{\text{JT}}$  [Eqs. (42) and (43)] produces vibronic wavefunctions (8) in the form  $|\Phi_{et}\rangle = |\chi_{et}^+\rangle|E_+\rangle + |\chi_{et}^-\rangle|E_-\rangle$  where:

$$|\chi_{et}^\pm\rangle = \sum_{\mathbf{n}l} C_{et;\mathbf{n}_1l_1\ldots\mathbf{n}_Nl_N}^\pm |n_1l_1, \ldots, n_Nl_N\rangle. \quad (49)$$

In terms of the wavefunctions  $|\chi_{et}^\pm\rangle$  the overlap integrals that appear in the expression for  $A_e(\hbar\omega)$  in Eqs. (14)

and (16) can be rewritten as

$$|\langle\chi_{gr}^e|\chi_{et}^{e_x}\rangle|^2 + |\langle\chi_{gr}^e|\chi_{et}^{e_y}\rangle|^2 = |\langle\chi_{gr}^e|\chi_{et}^+\rangle|^2 + |\langle\chi_{gr}^e|\chi_{et}^-\rangle|^2.$$

In the limit of zero temperature overlaps for luminescence spectrum (14) are calculated between the lowest vibronic state of the electronic ground state  $|^3A_2\rangle$  and all the vibrational states of the electronic excited state  $|^3E\rangle$ . The lowest vibronic state is always the one with the “pseudo spin”  $j = \pm\frac{1}{2}$  [29]. Therefore, in the case of luminescence one has to diagonalize the Hamiltonian for either the  $j = \frac{1}{2}$  or the  $j = -\frac{1}{2}$  “channel” (the two states are degenerate).

In the case of absorption, overlap integrals in the spectral function (16) are calculated between zero-phonon state  $|00..0\rangle$  of the electronic ground state  $|^3A_2\rangle$  and vibronic states of the electronic excited state  $|^3E\rangle$ . Overlaps will be non-zero only for vibronic states in the  $|^3E\rangle$  manifold that contain the contribution of the zero-phonon state  $|00..0\rangle$ . This phonon state is only present in vibronic states with  $j = \pm\frac{1}{2}$  [51], and therefore in our diagonalization procedure we again need to consider either only the  $j = \frac{1}{2}$  or the  $j = -\frac{1}{2}$  “channel”.

As in the case of spectral functions  $A_{a_1}(\hbar\omega)$ , when calculating  $A_e(\hbar\omega)$  we choose the vibrational modes and frequencies of the ground state for luminescence, and those of the excited state for absorption.

### D. Diagonalization of the vibronic Hamiltonian

Reformulation of the problem in terms of the new basis makes the diagonalization of the vibronic Hamiltonian in the presence of a *small* number of  $e$  modes a computationally tractable task. Without this reformulation, treating even a few modes would be computationally too expensive. In constructing the basis set we limit the total number of excited vibrations  $n_{\text{tot}} = \sum_k n_k$  to a certain number. By increasing this number we can monitor the convergence of the final result. We find that convergence is easily achieved in our case.

However, we are still facing a daunting challenge: for the NV center effectively an infinite number of  $e$  modes, described by the spectral density  $S_e(\hbar\omega)$ , participate in the Jahn–Teller effect. To address this problem we propose the following approach.

We approximate the actual spectral density  $S_e(\hbar\omega)$  with  $S_e^{(\text{eff})}(\hbar\omega)$ , defined as:

$$S_e^{(\text{eff})}(\hbar\omega) = \sum_{n=1}^{N_{\text{eff}}} \bar{K}_n^2 g_\sigma(\hbar\omega_n - \hbar\omega), \quad (50)$$

Here  $g_\sigma$  is a Gaussian function of width  $\sigma$ ; the sum runs over  $N_{\text{eff}}$  “effective” vibrations with frequencies  $\omega_n$  and vibronic coupling strengths  $\bar{K}_n^2$ . For a fixed number  $N_{\text{eff}}$ , the parameters  $\bar{K}_n^2$ ,  $\omega_n$ , and  $\sigma$  are obtained by the minimization of the integral

$$I = \int_0^\infty |S_e(\hbar\omega) - S_e^{(\text{eff})}(\hbar\omega)| d(\hbar\omega) \quad (51)$$

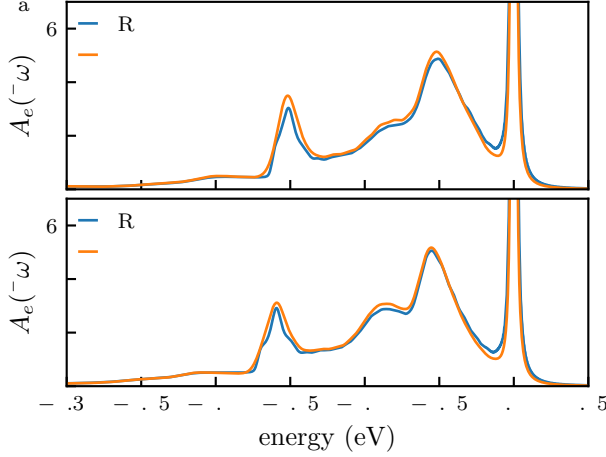


FIG. 8. The spectral function  $A_e(\hbar\omega)$  (in units  $1/\text{eV}$ ) for emission [Eq. (14)] obtained with (a) PBE and (b) HSE functionals. We compare spectral functions obtained via the solution of the multi-mode Jahn-Teller problem (“JT”) and via the Huang-Rhys treatment (“HR”).

while enforcing that  $\sum_{n=1}^{N_{\text{eff}}} \bar{K}_n^2 = \sum_{k=1}^N K_k^2 = S_e$ . If  $N_{\text{eff}} = N$ , the actual number of  $e$  doublets, then this approach reproduces the full calculation. However, one expects that convergence of the final result can be achieved for  $N_{\text{eff}} \ll N$ , such that the problem is still tractable by the diagonalization procedure. This indeed turns out to be the case. In Sec. III of the Supplemental Material we present a test of the procedure for the  $2 \times 2 \times 2$  supercell.

### E. Spectral functions $A_e(\hbar\omega)$ for absorption and emission

In this Section we briefly discuss the spectral functions  $A_e(\hbar\omega)$  [Eqs. (14) and (16)] for both luminescence and absorption.

The results for luminescence are shown in Fig. 8 for both functionals. We used  $N_{\text{eff}} = 22$  (cf. Sec. VIID). In the figure we compare  $A_e(\hbar\omega)$  obtained via the solution of the multi-mode JT problem (labeled “JT”) with the one obtained via the Huang-Rhys approach (labeled “HR”). In the latter we treat the  $e$  modes as if they were fully symmetric  $a_1$  modes. Spectral functions are obtained in a manner completely identical to those of  $a_1$  modes, as described in Sec. VI.

Somewhat surprisingly, the HR calculation yields spectral functions very similar to those of the JT calculation. The agreement between the two sets of calculations is striking and one is tempted to conclude that there is a deeper underlying reason for this. However, in Appendix A we show that the good agreement is to some degree accidental. Indeed, using first-order perturbation theory we derive that for  $S_e \ll 1$  the JT theory yields an intensity for the first vibrational side-peak exactly twice as large as the HR approach. As a result, the weight of

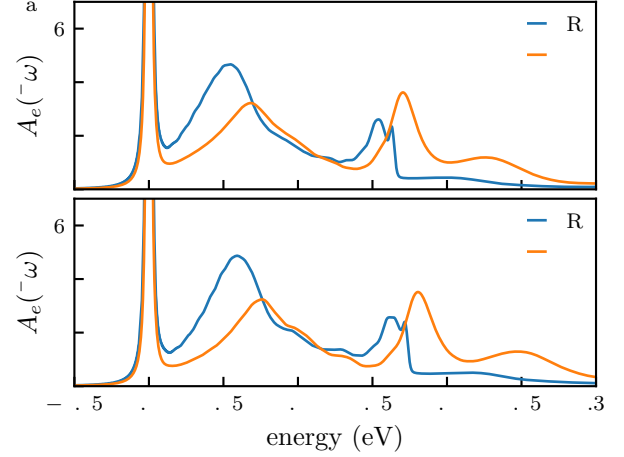


FIG. 9. The spectral function  $A_e(\hbar\omega)$  (in units  $1/\text{eV}$ ) for absorption [Eq. (16)] obtained with (a) PBE and (b) HSE functionals. We compare spectral functions obtained via the solution of the multi-mode Jahn-Teller problem (“JT theory”) and via the Huang-Rhys treatment (“HR theory”).

the ZPL is *smaller* in the JT treatment. We then use a simple model to show that as  $S_e$  becomes larger, the situation is reversed: the weight of the first phonon peak becomes smaller in the JT calculation with respect to the HR result, and vice versa for the weight of the ZPL. Interestingly, in the range  $S_e \approx 0.5 - 1.0$  the two approaches provide a very similar quantitative description, explaining the result shown in Fig. 8. Regardless, our analysis warns that applying the Huang-Rhys approach can lead to errors in the case of small  $S_e$ .

The spectral functions  $A_e(\hbar\omega)$  for absorption are shown in Fig. 9. In contrast to luminescence, the Jahn-Teller treatment differs substantially from the Huang-Rhys calculation. Overall, compared to the HR function, the JT function is “stretched”. This is in agreement with model calculations for systems with the dynamic JT effect [51], as also exemplified in recent first-principles modelling of diamondoids [53]. Moreover, we observe a change in the energy and the intensity of peaks that appear in  $A_e(\hbar\omega)$ . For example, the phonon side peak closest to the ZPL decreases in intensity and moves to larger energies. These results clearly illustrate that using the JT theory is essential in the case of absorption at NV centers in diamond.

## VIII. RESULTS: $A_1$ AND $E$ MODES COMBINED

In this Section we present the final result of our calculated, luminescence and absorption lineshapes, obtained via Eqs. (12), (17), and (18), and compare them with experimental lineshapes [54]. In Table IV the calculated Huang-Rhys factors for the coupling with  $a_1$  and  $e$  modes are summarized. We define the total Huang-Rhys factor as  $S_{\text{tot}} = S_{a_1} + S_e$ . In comparison with experiment, the

TABLE IV. Calculated Huang–Rhys factors for emission and absorption.

	Luminescence			Absorption		
	$S_{a_1}$	$S_e$	$S_{\text{tot}}$	$S_{a_1}$	$S_e$	$S_{\text{tot}}$
PBE	2.39	0.52	2.91	2.60	0.51	3.11
HSE	3.20	0.56	3.76	3.59	0.57	4.16
expt.			3.49 <sup>a</sup>			

<sup>a</sup> Reference 55

total Huang–Rhys factor for emission is slightly underestimated in PBE and overestimated in HSE. The contribution of  $e$  modes to optical lineshapes can be quantified by a ratio  $S_e/S_{\text{tot}}$ , which we find to be 14 – 18 %.

### A. Luminescence

The calculated luminescence lineshapes are compared to experimental curves from Refs. 55 (labeled “ANU”) and 8 (labeled “UCSB”) in Fig. 10. Details about experimental procedures and samples are given in the corresponding papers. To allow for a meaningful comparison the theoretical lineshapes were shifted to match the experimental ZPL. The overall agreement is quite good with both the PBE and the HSE functional. As one of the goals of the current paper is the analysis of the accuracy of modern density functionals in describing these luminescence lineshapes, we now discuss the differences between the two sets of calculations.

Comparing experiment with the PBE calculation, we see that the intensities of the ZPL and the first two phonon peaks in the calculated lineshape are too large. This is because the total HR factor calculated in PBE is smaller than the experimental one (Table IV). In contrast, the total HR factor calculated in HSE is larger than the experimental one (Table IV), yielding the intensity of the ZPL and the three phonon side peaks too small in comparison with experiment. From the atomistic point of view, one could conclude that the change in the equilibrium defect geometry between the ground and the excited states is slightly underestimated in PBE, while this change is overestimated in HSE.

Looking at the position of the peaks, we see, however, that theory agrees with experiment remarkably well. This concerns not only the main phonon replica at about 65 meV, but even the fine structure of the luminescence lineshape, especially visible between the second and the third replica of the 65 meV peak. We do note that the positions of the peaks in PBE (which are directly related to the vibrational frequencies) show a very close agreement with experiment, while some shifts are evident for HSE, because frequencies are slightly overestimated. This conclusion is in line with the fact that PBE does a better job at describing the lattice constant, bulk modulus, and bulk phonons of diamond (Sec. IV).

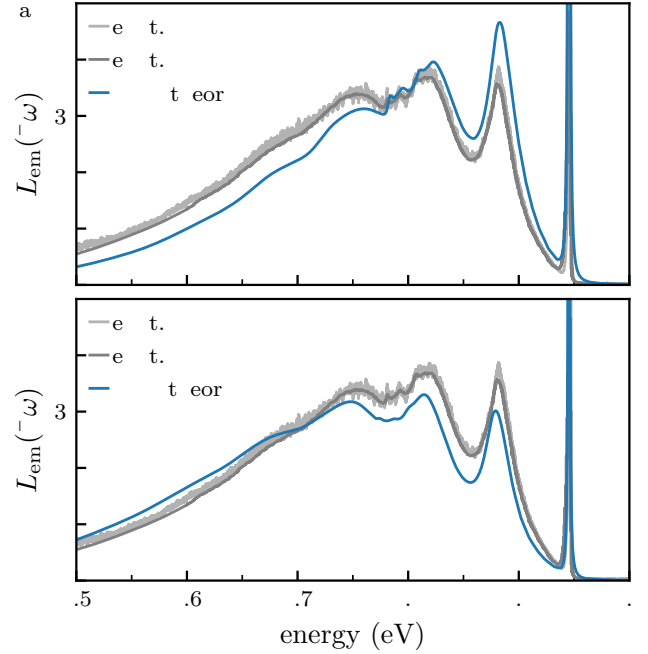


FIG. 10. Theoretical normalized luminescence lineshapes (in units 1/eV), compared with experimental spectra: (a) PBE functional; (b) HSE functional. Experimental spectra from Refs. 55 (labeled “ANU”) and 8 (labeled “UCSB”). The ZPL energy of the theoretical curves is set to the experimental value.

### B. Absorption

The calculated absorption lineshapes, where the contributions of both  $a_1$  and  $e$  phonons are included, are compared to experiment in Fig. 11. The experimental lineshape is from Ref. 54. As we did in the case of luminescence, we will first compare the overall lineshape and then look at the fine structure of the absorption band.

Comparing the PBE calculation [Fig. (11)(a)] with experiment we see that, like for luminescence, the intensity of both the ZPL and the first phonon side peak is overestimated in PBE. In contrast, both of these intensities are underestimated in HSE [Fig. (11)(b)]. Like in the case of luminescence, we trace this to the accuracy of the functionals in describing the change of the defect geometry in the ground state with respect to that of the excited state: the lattice relaxation is slightly underestimated in PBE, and overestimated in HSE.

Looking at the fine structure of the spectra, we see that, also on par with luminescence, the positions of the peaks are better described in PBE in comparison to HSE. This distinction is particularly clear in the description of the first phonon side peak, at  $\sim 2.1$  eV. The experimental curve displays the famous double-peak structure [45]. While the double peak is not clearly revealed in the PBE calculation, one can nevertheless see that the calculation accurately describes the overall position of the peak. In addition, the peak is broader than in the case of lumi-

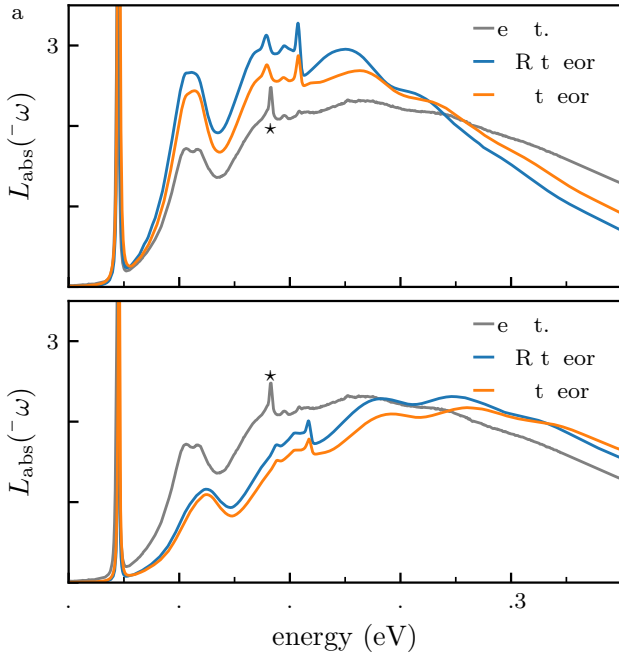


FIG. 11. Theoretical normalized absorption lineshapes (in units  $1/\text{eV}$ ) calculated using the Huang–Rhys (labeled ‘HR theory’) and Jahn–Teller treatment (labeled “JT theory”), compared with the experimental spectrum: (a) PBE functional; (b) HSE functional. The experiment is from Ref. 54. The ZPL energy of the theoretical curves is set to the experimental value. The small peak marked with a star “\*” in the experimental curve is the ZPL of another center and should be disregarded in the comparison.

nescence, in line with experimental findings. This peak is shifted to slightly larger energies in HSE. This can again be attributed to the fact that, like for bulk diamond and the NV center in the  $^3A_2$  state, the vibrational modes and frequencies in the  $^3E$  state are more accurately described in PBE. The origin of the double-peak structure will be addressed in a separate experimental–theoretical paper.

Focusing on the PBE result, it is interesting to compare the JT treatment with the HR treatment. Strictly speaking, the HR treatment for absorption is not justified in the presence of the dynamical JT effect. However, it can be viewed as an approximation, and is computationally much simpler. While the positions of peaks are reasonably well described in both treatments [Fig. 11(a)], there are distinct differences. For instance, the JT approach offers a better description of the two features at energies  $\sim 2.15$  and  $2.24$  eV. The improved agreement with experiment lends support to the validity of the multi-mode JT approach developed in our work.

### C. Summary of comparison with experiment

The main conclusions of our calculations, discussed in this Section, are:

(i) The change of the equilibrium defect geometry of the NV center in the  $^3E$  state with respect to the  $^3A_2$  state is overestimated in the HSE functional, while it is underestimated in the PBE functional.

(ii) Overall, both functionals describe the major peaks, as well as the fine structure in luminescence quite accurately. The positions of the peaks in the luminescence band calculated with the PBE functional are in nearly perfect agreement with the experimental spectrum, while the peak positions are overestimated (relative to the ZPL) in HSE.

(iii) The PBE functional describes the positions of major peaks and the fine structure in the absorption spectrum better than the HSE functional, and this is in particular visible in the width of the first phonon side peak.

(iv) Focusing on the PBE result, the Jahn–Teller theory provides a more accurate description of the peak positions in absorption, which is especially true in the case of the broad structure in the 2.1–2.3 eV range.

(v) The splitting of the first phonon side-peak in absorption is not clearly reproduced in theoretical calculations.

## IX. DISCUSSION

In this Section we critically review our methodology and the calculations, with a special emphasis on the accuracy of density functionals in the quantitative description of the vibrational and vibronic structure of isolated NV centers. Before we discuss the origin of the remaining discrepancies between theoretical and experimental curves (Figs. 10 and 11), let us mention some aspects that *have not* been addressed or that have only been partially addressed in our current paper:

*Quadratic interactions.* Our calculations rely on the linear theory of electron–phonon coupling. While there is little evidence that quadratic terms are important in the coupling to  $a_1$  phonons, it is known that quadratic Jahn–Teller terms do manifest themselves [12, 42]. In particular, it is estimated that the quadratic terms are  $\sim 1/3$  of the linear terms in terms of energy [12, 42]. Unfortunately, inclusion of quadratic terms in the multi-mode treatment increases the complexity of an already complex problem tremendously and it may not be possible to include this given current computational capabilities. We do suggest that more work is needed here.

*Treatment of the excited state.* The  $^3E$  excited state has been described using the  $\Delta$ SCF approach, as customary in state-of-the-art defect calculations [32, 56]. As demonstrated by our results,  $\Delta$ SCF yields good results, even though the calculation of excited states using constrained orbital occupations in DFT does not have the same fundamental backing of rigorous theorems as the calculation of the ground state. Future work in this field would certainly benefit from the ongoing developments in calculating excited states using more rigorous (and computationally much more intensive) many-body



approaches.

*Hessian matrices for charged defects.* There is a remaining question regarding the accuracy of Hessian matrix elements for charged defects in actual supercell calculations. In an infinite solid the negatively charged defect would induce polarization charge  $+(1 - 1/\epsilon)$  in the vicinity ( $\epsilon$  being the dielectric constant), while the polarization charge of the same magnitude but opposite polarity would be pushed to infinity. In the supercell approach the polarization charge that should be pushed to infinity is homogeneously distributed over the supercell [57] and there is, in addition, a neutralizing background that is introduced to prevent the Coulomb interaction from diverging. This “unphysical” spreading of the polarization charge and the presence of the neutralizing background may introduce errors in the calculation of force constants. Since these errors decrease as the size of the supercell grows, the approach employed in this work is to calculate these constants for the largest system that is tractable for both PBE and HSE functionals, *i.e.*, the  $4 \times 4 \times 4$  supercell nominally containing 512 items. A more rigorous solution of the issue is left for future work.

*Treatment of degenerate electronic states and dynamical Jahn-Teller effect.* As has been discussed in the literature, the application of DFT to degenerate electronic states ( ${}^3E$  in our case) is in principle more troublesome than in the case of non-degenerate ones [58], as the standard Hohenberg-Kohn theorem does not strictly apply. This also translates into practical aspects of finding vibrational frequencies and vibronic coupling constants. In this paper we chose specific approximations to determine these quantities, *i.e.*, determining the vibrational frequencies using the “symmetric” electron configuration  $a_1 e_x^{1.5} e_y^{1.5}$  and determining vibronic coupling constants from calculations performed away from the degeneracy point.

Let us assume that the aspects mentioned above affect the calculated lineshapes in a minor way. In this case one could attribute the remaining discrepancy between experiment and theory to the accuracy of density functionals in describing structural and vibrational properties of diamond and the NV center.

To test this hypothesis, let us assume that the shape of the calculated spectral densities  $S_{a_1}(\hbar\omega)$  and  $S_e(\hbar\omega)$ , calculated in PBE, is close to the “truth”, keeping in mind an excellent agreement regarding the positions of peaks, especially for luminescence. However, as discussed in Sec. VIII, atomic relaxations are slightly underestimated in PBE, the conclusion reached comparing the calculated Huang–Rhys factor with the experimental one. Let us assume that atomic relaxations projected on all vibrational modes are underestimated by the same linear factor  $\zeta^{1/2}$ . As a result, our estimate for “corrected” spectral densities are  $S'_{a_1}(\hbar\omega) = \zeta S_{a_1}(\hbar\omega)$  and  $S'_e(\hbar\omega) = \zeta S_e(\hbar\omega)$ .

In Fig. 12 we show the calculated luminescence lineshape with  $\zeta = 1.2$ ;  $\zeta$  was obtained via a least-square fit to the experimental luminescence lineshape. Unsurprisingly, this value is almost exactly the ratio between

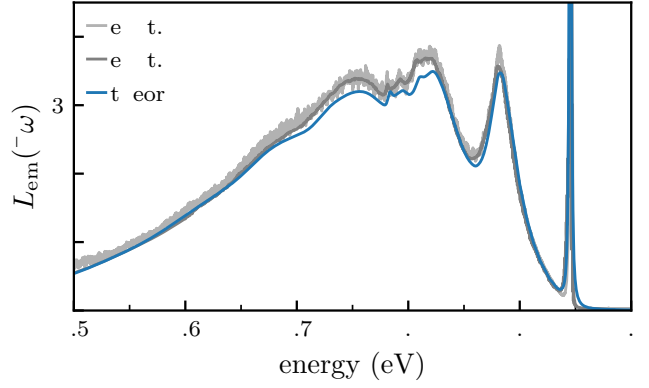


FIG. 12. Calculated normalized luminescence lineshape, compared with the experimental lineshape (both in units  $1/\text{eV}$ ). In the calculations we used scaled PBE spectral densities  $S'_{a_1} = \zeta S_{a_1}(\hbar\omega)$  and  $S'_e = \zeta S_e(\hbar\omega)$ , with  $\zeta = 1.2$ . Experimental spectra as in Fig. 10.

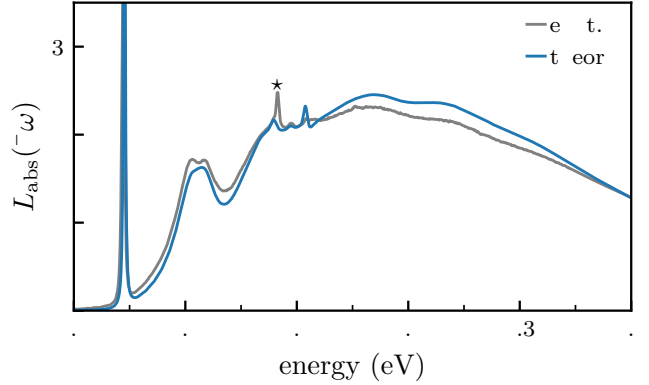


FIG. 13. (Color online) Calculated normalized absorption lineshape, compared with the experimental lineshape (both in units  $1/\text{eV}$ ). In the calculations we used scaled PBE spectral densities  $S'_{a_1} = \zeta S_{a_1}(\hbar\omega)$  and  $S'_e = \zeta S_e(\hbar\omega)$ , with  $\zeta = 1.2$ . Experimental spectrum as in Fig. 11. The experimental peak marked “\*” is the ZPL of another defect and should be disregarded in the comparison. The feature marked “#” in the calculated curve is discussed in the text.

the experimental total Huang–Rhys factor and the PBE value ( $3.49/2.91 = 1.199$ ; cf. Table IV). It is evident that the agreement with experiment is very good, both for the general shape of the luminescence line and for all the fine features of the spectrum.

Since the value of  $\zeta$  represents the scaling of the geometry relaxation in the excited state with respect to the ground state, we have to use the same value of  $\zeta$  for the calculation of the absorption lineshape. In other words, once  $\zeta$  is fixed based on an analysis of the luminescence lineshape, there are no more free parameters in the calculation of the absorption lineshape. Like for luminescence, in this calculation we use PBE spectral densities  $S_{a_1}(\hbar\omega)$  and  $S_e(\hbar\omega)$  scaled with  $\zeta$ :  $S'_{a_1}(\hbar\omega) = \zeta S_{a_1}(\hbar\omega)$  and  $S'_e(\hbar\omega) = \zeta S_e(\hbar\omega)$ . The result of the calculation is shown in Fig. 13. Like for luminescence, the general

shape is reproduced very well in the calculation. This good agreement lends support to the hypothesis that PBE calculations yield very good vibrational frequencies, but underestimate geometry relaxation.

Nevertheless, we see small discrepancies. For example, the calculation shows a small peak at 2.11 eV, indicated by “#” in the plot. It originates from a localized phonon mode just above the bulk phonon spectrum (less than 1 meV in our calculations), and this small peak seems to be absent in the experimental spectrum. [Interestingly, a localized phonon mode just above the bulk band has been observed in the infrared absorption spectrum for the  ${}^1E \rightarrow {}^1A_1$  transition [55] (cf. Fig. 1), even though, clearly, different electronic states are involved in that transition.] This localized mode is present in both PBE and HSE calculations (Fig. 11). The energy of this localized mode is very sensitive to the parameters of our calculations and its localized nature might be an artefact. Despite these two issues, the calculations show very good agreement with experiment. In particular, if we look at the *asymmetry* of luminescence and absorption lineshapes in experiment, we see that this asymmetry is reproduced very well.

We are now in the position to discuss why the luminescence lineshape, presented in our previous work (Ref. 8), already showed good agreement with the experimental curve, in spite of the fact that the methodology in that study was not as sophisticated as what is presented in the current work. The good agreement in Ref. 8 was largely due to fortuitous cancellation of two factors. (i) In Ref. 8 only the coupling to symmetric modes  $a_1$  was considered. As we now know from Table IV, the contribution of  $e$  modes to luminescence is  $\sim(16\text{--}18)\%$ . Neglect of  $e$  modes should have led to an underestimation of the theoretical Huang–Rhys factor compared to the experimental one. (ii) In Ref. 8, forces were calculated with HSE, but vibrational frequencies of the defect system were calculated using PBE, due to the high computational cost of HSE. Vibrational frequencies in HSE are higher than in PBE, as we have seen in the current work. Thus, using HSE forces with PBE frequencies in Eqs. (25) and (33) leads to an overestimation of partial Huang–Rhys factors for coupling to  $a_1$  modes. The two factors (i) and (ii) fortuitously compensated each other to a large degree, leading to a good agreement of the calculated lineshape with experiment.

## X. CONCLUSIONS

In conclusion, we have presented a theoretical study of the vibrational and vibronic structure of the negatively charged nitrogen–vacancy center in diamond. Our main focus was the calculation of luminescence and absorption lineshapes. We have approached the dilute limit by embedding the NV center in supercells of up to 64 000 atoms. This resulted in converged spectral densities of electron–phonon coupling throughout the whole

phonon spectrum. We have developed a computationally tractable methodology to account for the dynamical multi-mode Jahn–Teller effect, and have shown that the use of this methodology is particularly important when studying absorption at NV centers. Our calculations show that the vibrational structure determined with the PBE functional agrees slightly better with experiment than the one determined with the HSE functional. Nevertheless, the geometry relaxation between the two electronic states of the NV center is slightly underestimated in PBE, and slightly overestimated in HSE (judging from the comparison of the calculated total Huang–Rhys factor with the experimental one). This indicates that, while being overall accurate, presently available density functionals are still not “perfect” for describing subtle features in optical lineshapes. We can obtain excellent agreement with experiment for both luminescence and absorption by using PBE spectral densities of electron–phonon coupling but scaling them with a factor  $\zeta = 1.2$ .

Looking forward, our work indicates that the continuing development of more accurate density functionals, as well as computational advances for a rigorous but tractable treatment of excited states will be an essential feature of *quantitative* first-principles calculations for point defects. The methodology presented here advances first-principles calculations of electron–phonon coupling [59] for defects and will be useful in the study and identification of other point defects in solids. In particular, it is our hope that the methodology will help in identifying and designing [60] new quantum defects.

## ACKNOWLEDGMENTS

This work has received funding from the European Union’s Horizon 2020 research and innovation programme under grant agreement No. 820394 (project ASTERISQs). MD and NBM acknowledge funding from the Australian Research Council (DE170100169 and DP170103098). CGVdW was supported by the National Science Foundation (NSF) through Enabling Quantum Leap: Convergent Accelerated Discovery Foundries for Quantum Materials Science, Engineering and Information (Q-AMASE-i) (DMR-1906325). AA acknowledges the NSF Materials Research Science and Engineering Centers (MRSEC) Program (DMR-1720256) (Seed), and NSF Q-AMASE-i (DMR-1906325) for funding visits to the University of California. Computational resources were provided by the High Performance Computing Center “HPC Saulėtekis” in the Faculty of Physics, Vilnius University, the Extreme Science and Engineering Discovery Environment (XSEDE), which is supported by the NSF (ACI-1548562), and the National Computational Infrastructure (NCI), which is supported by the Australian Government.

## Appendix A: Comparison of Jahn–Teller and Huang–Rhys treatment in emission

In Sec. VII we have shown that in the case of luminescence at  $T = 0$  K the spectral functions  $A_e(\hbar\omega)$  calculated by means of the diagonalization of the vibronic Hamiltonian, on the one hand, and based on a simpler Huang–Rhys approach, on the other, are very close to each other (Fig. 8). In this Appendix we provide a rationale for this behavior and show that the agreement is to a large degree accidental for the NV center.

Let us consider a single  $e$  doublet with frequency  $\omega$ . In the notation of Sec. VII the harmonic part of the Hamiltonian is [cf. Eq. (36)]

$$\hat{H}_0 = \hat{C}_z \sum_{\gamma \in x,y} \left( -\frac{\hbar^2}{2} \frac{\partial^2}{\partial Q_\gamma^2} + \frac{1}{2} \omega^2 Q_\gamma^2 \right). \quad (\text{A1})$$

The linear Jahn–Teller interaction, Eq. (37), can be rewritten employing the parameter  $S_e$  introduced in Sec. VII as:

$$\hat{H}_{\text{JT}} = \sqrt{2S_e \hbar \omega^3} \left( \hat{C}_x Q_x + \hat{C}_y Q_y \right). \quad (\text{A2})$$

When the Jahn–Teller interaction is weak,  $S_e \ll 1$ , one can apply first-order perturbation theory. The ground-state eigenfunctions of the unperturbed Hamiltonian, Eq. (A1), are  $|00; E_\pm\rangle$  in the notation of Sec. VII. They correspond to two angular momentum components  $j = \pm \frac{1}{2}$ . As the total vibronic Hamiltonian for different values of  $j$  is decoupled, we can apply a simple non-degenerate perturbation theory to obtain first-order corrections of ground-state vibronic wavefunctions due to the presence of Jahn–Teller interactions Eq. (A2):

$$|\chi_0^{\text{JT}}; j = \pm \frac{1}{2}\rangle = \mathcal{A} \left( |00; E_\pm\rangle - \sqrt{2S_e} |1 \pm 1; E_\mp\rangle \right). \quad (\text{A3})$$

Here  $\mathcal{A} = 1/\sqrt{1+2S_e}$  is the normalization factor.

Our goal is to compare the JT treatment with the HR treatment. Therefore, we need to find a Hamiltonian of the type Eq. (23) that would yield the same Huang–Rhys factor  $S_e$  as above. There are many ways to achieve this; the final result is independent of this choice. One particular realization is

$$\hat{H}_{\text{HR}} = \hat{C}_z \sqrt{S_e \hbar \omega^3} (Q_x + Q_y), \quad (\text{A4})$$

to be compared with Eq. (A2). We will treat this as a perturbation to the Hamiltonian Eq. (A1). The linear-coupling of this form does not couple the two orbital states, so we can only consider the vibrational part of the wavefunction. Using the  $|n_x n_y\rangle$  basis for our vibrational states, we find that first-order perturbation theory gives

wavefunctions:

$$|\chi_0^{\text{HR}}\rangle = \mathcal{A} \left( |00\rangle - \sqrt{\frac{S_e}{2}} |10\rangle - \sqrt{\frac{S_e}{2}} |01\rangle \right). \quad (\text{A5})$$

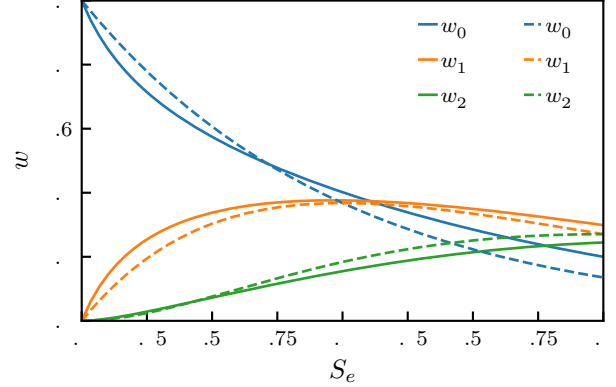


FIG. 14. Intensities of the zero-phonon line ( $w_0$ ) and the first two phonon replicas ( $w_1$  and  $w_2$ ) in the JT (solid lines) and the HR (dashed lines) treatments as a function of the Huang–Rhys factor  $S_e$ .

with the normalization factor  $\mathcal{A} = 1/\sqrt{1+S_e}$ .

Using the above expressions we can now derive the intensity of the first phonon replica (labeled  $w_1$ ) in the normalized luminescence spectrum. When  $S_e \ll 1$ , we get:

$$w_1^{\text{JT}} = \frac{2S_e}{1+2S_e} = 2S_e + O(S_e^2)$$

$$w_1^{\text{HR}} = \frac{S_e}{1+S_e} = S_e + O(S_e^2).$$

Thus, for the same value of the parameter  $S_e$  the JT theory yields the intensity of the first phonon peak twice as large as the HR theory.

In Fig. 14 the analysis is extended for larger values of  $S_e$ , where we compare the intensity of the ZPL  $w_0$  as well as of the first two phonon replicas in the two theories. In the case of the HR theory an analytical result [Eq. (24)] was used, while numerical diagonalization of the vibronic Hamiltonian was performed for the JT theory. For very small  $S_e$ , the numerical results confirm the conclusions of the perturbation theory, i.e., that the intensity of the first phonon replica is twice as large in the JT treatment. However, for  $S_e \approx 0.5 - 1.0$ , the values of  $w_0$ ,  $w_1$ , and  $w_2$  are very close to each other. For example, for  $S_e = 0.75$   $w_0$  and  $w_1$  differ by less than 4%, while the values of  $w_2$  (which are smaller) differ by 15 %. The actual values of  $S_e$  for the NV center fall in this range (Table IV), rationalizing the similarity of the HR and JT treatments for luminescence. When  $S_e$  is increased above this range, the HR theory still performs rather well and can be considered as an approximation to the JT treatment. However, one should be extremely cautious applying the HR approach for JT systems with  $S_e < 0.5$ , especially if the focus is on the phonon sideband.

- 
- [1] K. Huang and A. Rhys, Theory of light absorption and non-radiative transitions in F-centres, *Proc. R. Soc. Lond. Series A* **204**, 406 (1950).
- [2] J. J. Markham, Interaction of normal modes with electron traps, *Rev. Mod. Phys.* **31**, 956 (1959).
- [3] I. S. Osad'ko, Determination of electron-phonon coupling from structured optical spectra of impurity centers, *Sov. Phys. Uspekhi* **22**, 311 (1979).
- [4] A. M. Stoneham, *Theory of defects in solids* (Oxford University Press, 2001).
- [5] R. M. Martin, *Electronic structure. Basic theory and practical methods* (Cambridge University Press, 2004).
- [6] M. Kretov, I. Iskandarova, B. Potapkin, A. Scherbinin, A. Srivastava, and N. Stepanov, Simulation of structured  ${}^4T_1 \rightarrow {}^6A_1$  emission bands of  $Mn^{2+}$  impurity in  $Zn_2SiO_4$ : A first-principle methodology, *J. Lumin.* **132**, 2143 (2012).
- [7] A. Alkauskas, J. L. Lyons, D. Steiauf, and C. G. Van de Walle, First-principles calculations of luminescence spectrum line shapes for defects in semiconductors: the example of GaN and ZnO, *Phys. Rev. Lett.* **109**, 267401 (2012).
- [8] A. Alkauskas, B. B. Buckley, D. D. Awschalom, and C. G. Van de Walle, First-principles theory of the luminescence lineshape for the triplet transition in diamond NV centres, *New J. Phys.* **16**, 073026 (2014).
- [9] C. Freysoldt, B. Grabowski, T. Hickel, J. Neugebauer, G. Kresse, A. Janotti, and C. G. Van de Walle, First-principles calculations for point defects in solids, *Rev. Mod. Phys.* **86**, 253 (2014).
- [10] M. W. Doherty, N. B. Manson, P. Delaney, F. Jelezko, J. Wrachtrup, and L. C. Hollenberg, The nitrogen-vacancy colour centre in diamond, *Phys. Rep.* **528**, 1 (2013).
- [11] K.-M. C. Fu, C. Santori, P. E. Barclay, L. J. Rogers, N. B. Manson, and R. G. Beausoleil, Observation of the dynamic Jahn-Teller effect in the excited states of nitrogen-vacancy centers in diamond, *Phys. Rev. Lett.* **103**, 256404 (2009).
- [12] G. Thiering and A. Gali, Ab initio calculation of spin-orbit coupling for an NV center in diamond exhibiting dynamic Jahn-Teller effect, *Phys. Rev. B* **96**, 081115(R) (2017).
- [13] A. Hashemi, C. Linderälv, A. V. Krashennnikov, T. Ala-Nissilä, P. Erhart, and H.-P. Komsa, Photoluminescence lineshapes for color centers in Silicon Carbide from density functional theory calculations, [arXiv:2010.01508](https://arxiv.org/abs/2010.01508) (2020), unpublished.
- [14] B. Bouquiaux, Y. Jia, S. Poncé, A. Miglio, M. Mikami, and X. Gonze, First-principles characterization of  $Sr[Li_2Al_2O_2N_2]:Eu^{2+}$  phosphor: insights into its narrow emission spectrum, [arXiv:2010.00423](https://arxiv.org/abs/2010.00423) (2020), unpublished.
- [15] R. Berger, C. Fischer, and M. Klessinger, Calculation of the vibronic fine structure in electronic spectra at higher temperatures. 1. Benzene and Pyrazine, *J. Phys. Chem. A* **102**, 7157 (1998).
- [16] M. Dierksen and S. Grimme, Density functional calculations of the vibronic structure of electronic absorption spectra, *J. Chem. Phys.* **120**, 3544 (2004).
- [17] R. Borrelli, A. Capobianco, and A. Peluso, Franck-Condon factors – computational approaches and recent developments, *Can. J. Chem.* **91**, 495 (2013).
- [18] M. C. M. O'Brien, The dynamic Jahn-Teller effect with many frequencies: a simple approach to a complicated problem, *J. Phys. C: Solid State Phys.* **5**, 2045 (1972).
- [19] G. Davies, The Jahn-Teller effect and vibronic coupling at deep levels in diamond, *Rep. Prog. Phys.* **44**, 787 (1981).
- [20] F. S. Ham, Effect of linear Jahn-Teller coupling on paramagnetic resonance in a  ${}^2E$  state, *Phys. Rev.* **166**, 307 (1968).
- [21] M. C. M. O'Brien and S. N. Evangelou, The calculation of absorption band shapes in dynamic Jahn-Teller systems by the use of the Lanczos algorithm, *J. Phys. C: Solid State Phys.* **13**, 611 (1980).
- [22] D. D. Awschalom, R. Hanson, J. Wrachtrup, and B. B. Zhou, Quantum technologies with optically interfaced solid-state spins, *Nat. Photonics* **12**, 516 (2018).
- [23] R. Schirhagl, K. Chang, M. Loretz, and C. L. Degen, Nitrogen-vacancy centers in diamond: Nanoscale sensors for physics and biology, *Annu. Rev. Phys. Chem.* **65**, 83 (2014).
- [24] L. Childress and R. Hanson, Diamond NV centers for quantum computing and quantum networks, *MRS Bull.* **38**, 134–138 (2013).
- [25] G. Waldherr, Y. Wang, S. Zaiser, M. Jamali, T. Schulte-Herbruggen, H. Abe, T. Ohshima, J. Isoya, J. F. Du, P. Neumann, and J. Wrachtrup, Quantum error correction in a solid-state hybrid spin register, *Nature* **506**, 204 (2014).
- [26] A. Alkauskas, M. D. McCluskey, and C. G. Van de Walle, Tutorial: Defects in semiconductors—combining experiment and theory, *J. Appl. Phys.* **119**, 181101 (2016).
- [27] M. Lax, The Franck-Condon principle and its application to crystals, *J. Chem. Phys.* **20**, 1752 (1952).
- [28] T. Azumi and K. Matsuzaki, What does the term “vibronic coupling” mean?, *Photochem. Photobiol.* **25**, 315 (1977).
- [29] I. B. Bersuker and V. Z. Polinger, *Vibronic interactions in molecules and crystals* (Springer, Berlin, 2012).
- [30] J. Heyd, G. E. Scuseria, and M. Ernzerhof, Hybrid functionals based on a screened Coulomb potential, *J. Chem. Phys.* **118**, 8207 (2003).
- [31] J. P. Perdew, K. Burke, and M. Ernzerhof, Generalized gradient approximation made simple, *Phys. Rev. Lett.* **77**, 3865 (1996).
- [32] A. Gali, E. Jánzén, P. Deák, G. Kresse, and E. Kaxiras, Theory of spin-conserving excitation of the  $N-V^-$  center in diamond, *Phys. Rev. Lett.* **103**, 186404 (2009).
- [33] K. Hummer, J. Harl, and G. Kresse, Heyd-Scuseria-Ernzerhof hybrid functional for calculating the lattice dynamics of semiconductors, *Phys. Rev. B* **80**, 115205 (2009).
- [34] G. Kresse and J. Furthmüller, Efficient iterative schemes for ab initio total-energy calculations using a plane-wave basis set, *Phys. Rev. B* **54**, 11169 (1996).
- [35] O. Madelung, *Semiconductors: group IV elements and III-V compounds* (Springer, 2012).
- [36] E. S. Zouboulis, M. Grimsditch, A. K. Ramdas, and S. Rodriguez, Temperature dependence of the elastic moduli of diamond: A Brillouin-scattering study, *Phys.*



- Rev. B* **57**, 2889 (1998).
- [37] J. Warren, J. Yarnell, G. Dolling, and R. Cowley, Lattice dynamics of diamond, *Phys. Rev.* **158**, 805 (1967).
  - [38] A. Togo and I. Tanaka, First principles phonon calculations in materials science, *Scr. Mater.* **108**, 1 (2015).
  - [39] S. A. Solin and A. K. Ramdas, Raman spectrum of diamond, *Phys. Rev. B* **1**, 1687 (1970).
  - [40] A. Gali, Ab initio theory of the nitrogen-vacancy center in diamond, *Nanophotonics* **8**, 1907 (2019).
  - [41] R. O. Jones and O. Gunnarsson, The density functional formalism, its applications and prospects, *Rev. Mod. Phys.* **61**, 689 (1989).
  - [42] T. A. Abtew, Y. Y. Sun, B.-C. Shih, P. Dev, S. B. Zhang, and P. Zhang, Dynamic Jahn-Teller effect in the NV<sup>-</sup> center in diamond, *Phys. Rev. Lett.* **107**, 146403 (2011).
  - [43] E. Londero, G. Thiering, L. Razinkovas, A. Gali, and A. Alkauskas, Vibrational modes of negatively charged silicon-vacancy centers in diamond from ab initio calculations, *Phys. Rev. B* **98**, 035306 (2018).
  - [44] G. Kresse, J. Furthmüller, and J. Hafner, Ab initio force constant approach to phonon dispersion relations of diamond and graphite, *EPL (Europhys. Lett.)* **32**, 729 (1995).
  - [45] G. Davies and M. Hamer, Optical studies of the 1.945 eV vibronic band in diamond, *Proc. R. Soc. Lond. Series A* **348**, 285 (1976).
  - [46] C. Campos and J. E. Roman, Strategies for spectrum slicing based on restarted Lanczos methods, *Numer. Algorithms* **60**, 279 (2012).
  - [47] V. Hernandez, J. E. Roman, and V. Vidal, SLEPc: A scalable and flexible toolkit for the solution of eigenvalue problems, *ACM Trans. Math. Softw.* **31**, 351 (2005).
  - [48] P. R. Amestoy, I. S. Duff, and J.-Y. L'Excellent, Multi-frontal parallel distributed symmetric and unsymmetric solvers, *Comput. Methods Appl. Mech. Eng.* **184**, 501 (2000).
  - [49] Y. Toyozawa, *Optical processes in solids* (Cambridge University Press, 2003).
  - [50] See Supplemental Material at [URL will be inserted by publisher] for a discussion about the decay of forces at NV centers, the choice of vibrational modes for the calculation of luminescence and absorption lineshapes, and benchmarking of the diagonalization of the Jahn-Teller Hamiltonian.
  - [51] H. C. Longuet-Higgins, U. Öpik, M. H. L. Pryce, and R. Sack, Studies of the Jahn-Teller effect. ii. The dynamical problem, *Proc. R. Soc. Lond. Series A* **244**, 1 (1958).
  - [52] C. Cohen-Tannoudji and B. Diu, *Quantum mechanics* (Wiley-VCH, 1986).
  - [53] A. Gali, T. Demján, M. Vörös, G. Thiering, E. Cannuccia, and A. Marini, Electron-vibration coupling induced renormalization in the photoemission spectrum of diamondoids, *Nature Communications* **7**, 11327 (2016).
  - [54] N. B. Manson, M. Hedges, M. S. J. Barson, R. Ahlfeldt, M. W. Doherty, H. Abe, T. Ohshima, and M. J. Sellars, NV<sup>-</sup>-N<sup>+</sup> pair centre in 1b diamond, *New J. Phys.* **20**, 113037 (2018).
  - [55] P. Kehayias, M. W. Doherty, D. English, R. Fischer, A. Jarmola, K. Jensen, N. Leefer, P. Hemmer, N. B. Manson, and D. Budker, Infrared absorption band and vibronic structure of the nitrogen-vacancy center in diamond, *Phys. Rev. B* **88**, 165202 (2013).
  - [56] C. E. Dreyer, A. Alkauskas, J. L. Lyons, A. Janotti, and C. G. Van de Walle, First-principles calculations of point defects for quantum technologies, *Annu. Rev. Mater. Res.* **48**, 1 (2018).
  - [57] C. Freysoldt, J. Neugebauer, and C. G. Van de Walle, Electrostatic interactions between charged defects in supercells, *Phys. Stat. Solidi B* **248**, 1067 (2011).
  - [58] I. B. Bersuker, Limitations of density functional theory in application to degenerate states, *J. Comput. Chem.* **18**, 260 (1997).
  - [59] F. Giustino, Electron-phonon interactions from first principles, *Rev. Mod. Phys.* **89**, 015003 (2017).
  - [60] L. Bassett, A. Alkauskas, A. Exarhos, and K.-M. Fu, Quantum defects by design, *Nanophotonics* **8**, 1867 (2019).

# Vibrational and vibronic structure of isolated point defects: the nitrogen-vacancy center in diamond. Supplemental material

Lukas Razinkovas, Marcus W. Doherty, Neil B. Manson, Chris G. Van de Walle, and Audrius Alkauskas

## I. DECAY OF FORCES

In Sec. VI of the main text we discussed the rapid decay of forces on the atoms surrounding the NV center when the electronic state is changed from  ${}^3E$  to  ${}^3A_2$  at the equilibrium geometry of the  ${}^3E$  state. This is illustrated in Fig. 1, which shows the force on the atom as a function of the distance from the nitrogen atom. In the figure we compare the results from two supercells:  $4 \times 4 \times 4$  (512 atomic sites) and  $5 \times 5 \times 5$  (1000 atomic sites). The largest forces are experienced by the carbon atoms around the vacant site and are slightly above 1000 meV/Å. However, forces quickly decay away from the NV center. At distances  $d > 7$  Å from the nitrogen atom the forces become smaller than 10 meV/Å. Importantly, we find that for atoms that are both closer than  $d = 7$  Å to the N site and those with forces  $F > 10$  meV/Å (upper left quadrant), the results from the two supercells fall on top of each other. This indicates that these forces are already converged as a function of the supercell size. For atoms at distances  $d < 7$  Å, but with forces  $F < 10$  meV/Å (lower left quadrant) the difference in forces is slightly larger, but the overall agreement is still very good. Supercell effects are much larger for atoms further than  $d = 7$  Å from the N atom, however, the forces on the atoms are very small. In our calculations we set all these forces to zero when calculating spectral densities. We estimate that the error associated with this approximation for calculated spectral densities and the total Huang-Rhys factor is  $< 1$  %.

The same reasoning as above holds for forces when the state is changed from  ${}^3A_2$  to  ${}^3E$  at the equilibrium geometry of the  ${}^3A_2$  state.

## II. CHOICE OF FREQUENCIES IN THE CALCULATION OF LUMINESCENCE AND ABSORPTION LINESHAPES

When calculating absorption and emission lineshapes in Secs. VI, VII, and VIII of the main text, we employed the equal-mode approximation, whereby the vibrational modes and frequencies in the ground and excited states were taken to be identical. In this Section we discuss the validity of this simplification. We stress at the outset that the

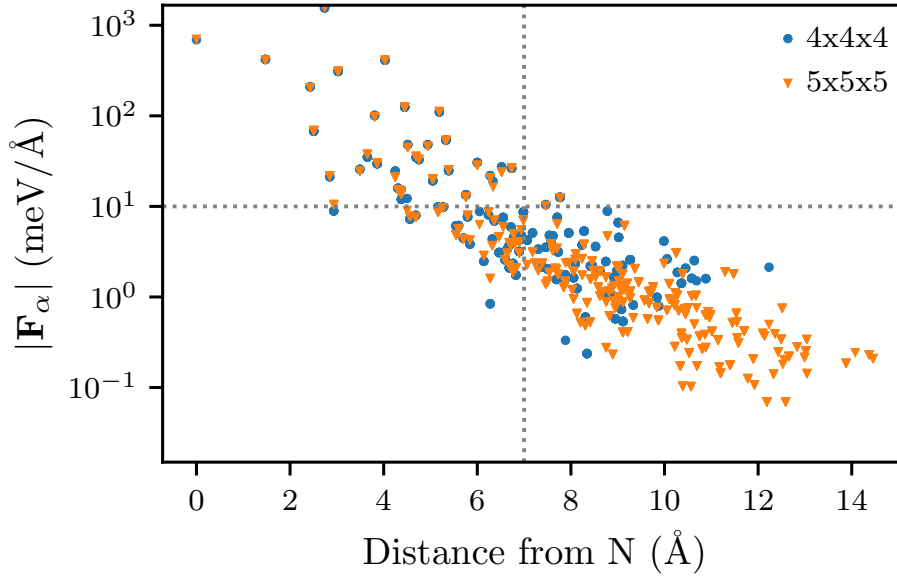


FIG. 1. Decay of forces on the atoms surround the NV center when the electronic state is changed from  ${}^3E$  to  ${}^3A_2$  at the equilibrium geometry of the  ${}^3E$  state. Results for two supercells are shown:  $4 \times 4 \times 4$  (512 atomic sites) and  $5 \times 5 \times 5$  (1000 atomic sites)

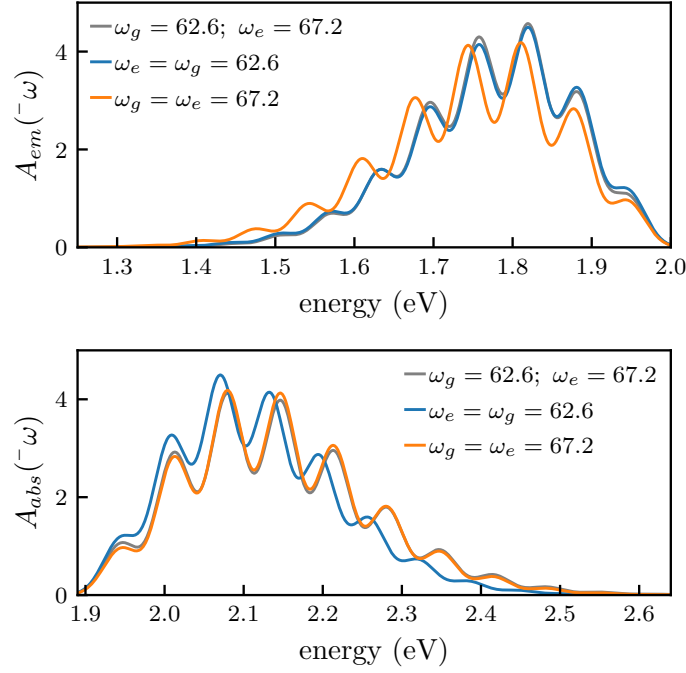


FIG. 2. Spectral functions (in 1/eV) for luminescence (a) and absorption (b) in the 1D approximation. Gray: using actual frequencies in the ground and the excited state; blue: using the frequency of the ground state; orange: using the frequency of the excited state. The ZPL energy was set to the experimental value,  $E_{ZPL} = 1.945$  eV, and a smearing parameter  $\sigma = 25$  meV was used.

validity of the approximation can be rigorously tested only in systems with a small number of vibrational degrees of freedom, where the exact calculation is possible (see, e.g., Fig. 2 in Ref. 1). Here we resort to a qualitative analysis.

The difference between the two sets of modes can be quantified by calculating the average frequency of modes that contribute to the optical lineshapes. This average is defined as:

$$\Omega_{\{e,g\}}^2 = \frac{\sum_k \omega_{\{e,g\};k}^2 \Delta Q_k^2}{\sum_k \Delta Q_k^2}. \quad (1)$$

The sum runs over all vibrational modes of  $a_1$  and  $e$  symmetry.  $\Delta Q_k$  is defined in Eq. (31) of the main text for  $a_1$  modes and an analogous set of equations Eqs. (45) and (46) of the main text for  $e$  modes. We obtain  $\hbar\Omega_g = 62.6$  meV and  $\hbar\Omega_e = 67.2$  meV for average frequencies in the ground and the excited state. This result indicates that the frequencies of modes that contribute to optical lineshapes are on average higher in the excited state than in the ground state.

Having determined average frequencies we can now calculate luminescence and absorption lineshapes in a model system of one-dimensional quantum harmonic oscillators described by these frequencies (see Ref. 1 for more details). In Fig. 2 we compare the lineshapes calculated using the actual frequencies that are different for ground and excited states, with two approximations: in the first approximation the two frequencies are taken to coincide with that of the ground state  $\hbar\Omega_g = 62.6$  meV (orange lines), while in the second approximation they coincide with that of the excited state  $\hbar\Omega_e = 67.2$  meV (green lines). The results show that the “true” lineshape is approximated extremely well by setting the frequency to that of the *final* state: *i.e.*, the ground state in the case of luminescence, and the excited state in the case of absorption. In contrast, setting the frequency to that of the initial state does a poor job.

### III. BENCHMARKING THE DIAGONALIZATION OF THE JAHN-TELLER HAMILTONIAN

In this Section we illustrate the procedure of the diagonalization of the Jahn-Teller Hamiltonian outlined in Sec. VII D of the main text in the case of the  $2 \times 2 \times 2$  fcc supercell, for which it is possible to diagonalize the vibronic Hamiltonian including all 62  $e$  doublets. In Fig. 3 we show the approximation of  $S_e(\hbar\omega)$  with  $S_e^{(\text{eff})}(\hbar\omega)$  for  $N_{\text{eff}} = 2, 4, 8$  [Eq. (49) of the main text]. We see that in the case of  $N_{\text{eff}} = 8$  the approximate spectral density  $S_e^{(\text{eff})}(\hbar\omega)$  is indistinguishable from the real spectral density  $S_e(\hbar\omega)$ .

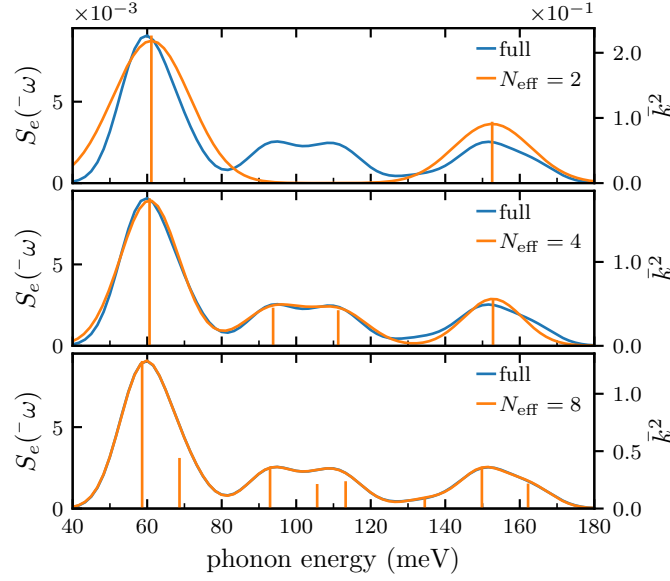


FIG. 3. Convergence of  $S_e^{(\text{eff})}(\hbar\omega)$  towards  $S_e(\hbar\omega)$  [Eq. (49) of the main text] when increasing the number of effective modes  $N_{\text{eff}}$ . The results are for the NV center in the  $2 \times 2 \times 2$  supercell. Spectral densities in units  $1/\text{meV}$ .

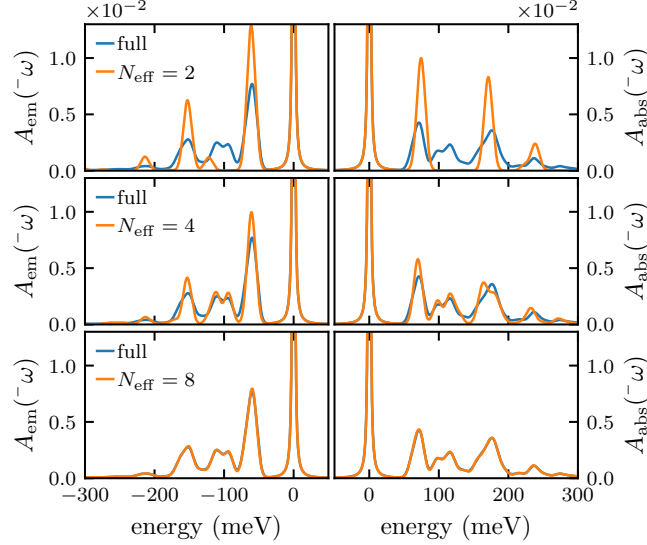


FIG. 4. Convergence of the spectral function  $A_e(\hbar\omega)$  [in units  $1/\text{meV}$ ] for emission (left) and absorption (right) as a function of  $N_{\text{eff}}$ , the number of effective  $e$  modes included in the calculation. The results are for the NV center in the  $2 \times 2 \times 2$  fcc supercell.

For the diagonalization of the Jahn-Teller Hamiltonian we use  $n_{\text{tot}} = 3$ . Although this basis is not converged with respect to  $n_{\text{tot}}$ , it is sufficient for benchmarking purposes, as we keep  $n_{\text{tot}}$  the same for all calculations with effective modes. The resulting spectral functions  $A_e(\hbar\omega)$  for absorption and emission, calculated from  $S_e^{(\text{eff})}(\hbar\omega)$ , are compared to the ones calculated from  $S_e(\hbar\omega)$  that include *all* vibrations for the given supercell in Fig. 4. We see that the result with  $N_{\text{eff}} = 8$  reproduces the full result very accurately. Note that the spectral function  $S_e(\hbar\omega)$  for the  $2 \times 2 \times 2$  supercell is not yet converged with respect to the supercell size. The purpose of Fig. 4 is to illustrate our methodology for the largest supercell for which the full calculation is still possible.